Quaternary Geochronology xxx (2010) 1–18

Contents lists available at ScienceDirect

Quaternary Geochronology

journal homepage: www.elsevier.com/locate/quageo

Research Paper

In situ cosmogenic ^{10}Be production-rate calibration from the Southern Alps, New Zealand

A.E. Putnam [a,*], J.M. Schaefer [b], D.J.A. Barrell [c], M. Vandergoes [d], G.H. Denton [a], M.R. Kaplan [b], R.C. Finkel [e,f], R. Schwartz [b], B.M. Goehring [b], S.E. Kelley [a]

[a] Department of Earth Sciences and Climate Change Institute, University of Maine, Orono, ME 04469, USA
[b] Lamont-Doherty Earth Observatory, Palisades, NY 10964, USA
[c] GNS Science, Dunedin, New Zealand
[d] GNS Science, Lower Hutt, New Zealand
[e] Earth and Planetary Science Dept, University of California, Berkeley, CA 94720, USA
[f] ASTER, Centre Européen de Recherche et Enseignement des Géosciences de l'Environnement, Aix-en-Provence 13100, France

ARTICLE INFO

Article history:
Received 12 June 2009
Received in revised form
17 November 2009
Accepted 2 December 2009
Available online xxx

Keywords:
^{10}Be
Production rate
Cosmogenic nuclide
^{14}C
Moraine
Debris flow
Holocene
Last glacial maximum
South Island

ABSTRACT

We present a ^{10}Be production-rate calibration derived from an early Holocene debris-flow deposit at about 1000 m above sea level in the central Southern Alps, New Zealand, in the mid-latitude Southern Hemisphere. Ten radiocarbon ages on macrofossils from a soil horizon buried by the deposit date the deposit to 9690 ± 50 calendar years before AD2008. Surface ^{10}Be concentrations of seven large boulders partially embedded in the stable surface of the deposit are tightly distributed, yielding a standard deviation of ~2%. Conversion of the ^{10}Be measurements to sea level/high-latitude values using each of five standard scaling methods indicates ^{10}Be production rates of 3.84 ± 0.08, 3.87 ± 0.08, 3.83 ± 0.08, 4.15 ± 0.09, and 3.74 ± 0.08 atoms g^{-1} a^{-1}, relative to the '07KNSTD' ^{10}Be AMS standard, and including only the local time-integrated production-rate uncertainties. When including a sea level high-latitude scaling uncertainty the overall error is ~2.5% (1σ) for each rate. To test the regional applicability of this production-rate calibration, we measured ^{10}Be concentrations in a set of nearby moraines deposited before 18 060 ± 200 years before AD2008. The ^{10}Be ages are only consistent with minimum-limiting ^{14}C age data when calculated using the new production rates. This also suggests that terrestrial in situ cosmogenic-nuclide production did not change significantly from Last Glacial Maximum to Holocene time in New Zealand. Our production rates agree well with those of a recent calibration study from northeastern North America, but are 12–14% lower than other commonly adopted values. The production-rate values presented here can be used elsewhere in New Zealand for rock surfaces exposed during or since the last glacial period.

1. Introduction

Surface-exposure dating using in situ cosmogenic nuclides has developed into a revolutionary tool for understanding Earth surface processes. Improvements in laboratory procedures and accelerator mass spectrometry (AMS) have greatly enhanced the analytical precision of the method, but the application of surface-exposure dating to problems requiring sub-millennial-scale accuracy remains hampered by systematic uncertainties associated with terrestrial cosmogenic nuclide production rates. The rate at which a cosmogenic nuclide is produced in a rock at the earth's surface is required to convert a measured nuclide concentration into an exposure age (or erosion rate). The production rate of a particular cosmogenic nuclide can be evaluated by measuring the nuclide concentration in a rock whose exposure time has been well determined by independent means. In order to translate a production rate measured at one location to that at another location, local influences must be taken into account. Local influences on cosmogenic nuclide production include spatial and temporal variations in atmospheric pressure (e.g., Stone, 2000; Gosse and Phillips, 2001; Ackert et al., 2003; Licciardi et al., 2006; Staiger et al., 2007), time-dependent fluctuations of Earth's magnetic field (e.g., Nishiizumi et al., 1989; Dunai, 2001; Pigati and Lifton, 2004; Desilets and Zreda, 2003; Desilets et al., 2006; Lifton et al., 2005, 2008), and potential effects of solar modulation (Lifton et al., 2005). Exposure ages are thus calculated using a production rate obtained

* Corresponding author. Tel.: +1 207 581 2166; fax: +1 207 581 1203.
E-mail address: aaron.putnam@umit.maine.edu (A.E. Putnam).

1871-1014/$ – see front matter © 2009 Elsevier B.V. All rights reserved.
doi:10.1016/j.quageo.2009.12.001

from independently age-constrained calibration points, scaled to account for atmospheric pressure, geomagnetic, and solar modulation effects.

In this paper, we focus on ^{10}Be, which is the nuclide used most widely for exposure-dating applications. Over the last two decades, a network of production-rate calibration sites has been established (summarized in Balco et al., 2008), concentrated in the middle latitudes of the Northern Hemisphere and ranging up to 2000 m altitude. To produce a reference value, each local production rate has been scaled to sea level and high latitude (SLHL) using theoretical models that rely on neutron-monitor data (Dunai, 2001; Desilets et al., 2006; Lifton et al., 2005) or on a combination of neutron detectors and nuclear disintegration data (e.g., Lal and Peters, 1967; Lal, 1991). In general, scaling models predict a threefold production-rate increase from sea level to 1500 m altitude, and a twofold increase from the equator to the poles at sea level. Uncertainties of the 'global ^{10}Be calibration dataset' are about 9–12%, if one considers uncertainties in both local production rates and in scaling (Balco et al., 2008).

One way to improve the accuracy of surface-exposure chronologies is to obtain high-precision ^{10}Be production rates from local calibration sites. This is of particular importance for Southern Hemisphere applications of the ^{10}Be method, where there is an abundance of in situ cosmogenic ^{10}Be measurements (e.g., Shulmeister et al., 2005; Schaefer et al., 2006, 2009; Sutherland et al., 2007; Barrows et al., 2007; Ackert et al., 2008; Kaplan et al., 2008), but no calibration sites for this nuclide. Thus, ^{10}Be ages calculated from the southern latitudes depend on production rates from sites in the Northern Hemisphere that are extrapolated to the Southern Hemisphere using different scaling schemes. Therefore, ages calculated in the Southern Hemisphere incorporate difficult-to-quantify uncertainties stemming from how these scaling models describe nuclide production at locations distant from given calibration points (e.g., Dunai, 2001; Lifton et al., 2005, 2008; Desilets et al., 2006)

Here we document a ^{10}Be production-rate calibration site from the Southern Hemisphere middle latitudes. This site at Macaulay River, South Island, New Zealand, comprises a bouldery debris-flow deposit that overran a vegetated alluvial terrace in the early Holocene. We report high-precision measurements of ^{10}Be concentrations in boulders protruding from the top of this debris-flow landform. We determine the age of the deposit by ^{14}C dating of macrofossils from buried vegetation and soil that directly underlie the debris-flow deposit. The date of burial of these organic materials defines the age of the debris flow and the commencement of ^{10}Be accumulation in surface boulders. From these data we derive an SLHL in situ production rate for ^{10}Be at this location. We then examine the validity of this production-rate estimate by obtaining ^{10}Be measurements from boulders partially embedded in the surface of a nearby moraine sequence (Boundary Stream) deposited during the Last Glacial Maximum (LGM). Radiocarbon-dated sediments within a pond dammed by ice-marginal deposits afford a minimum-limiting age of these moraines. Using this approach, we discuss the implication for variations of the ^{10}Be production rate over the last glacial–interglacial transition in New Zealand.

2. Geologic description

New Zealand is the emergent part of a largely submerged block of continental rock straddling the boundary between the Australian and Pacific plates. Through South Island, the Alpine Fault marks the plate boundary, where plate motion is expressed as strike-slip displacement with a minor reverse component. Uplift southeast of the Alpine Fault has produced the Southern Alps. The study areas are on the eastern side of the Southern Alps (Fig. 1), within well-indurated Mesozoic sedimentary rocks dominated by 'greywacke' sandstone and 'argillite' mudstone. The highest parts of the Southern Alps support valley glaciers today, but during the LGM, and earlier glaciations, valley glaciers extended throughout the mountain range and out onto adjacent foreland regions.

2.1. Overview of the Macaulay valley

The Macaulay River is a tributary of Lake Tekapo (Fig. 1), the catchment of which was fully glaciated during the LGM. Well upstream of the LGM terminal moraine complex, the Macaulay valley contains ice-sculpted bedrock valley sides, trimlines, hanging tributary valleys and patches of recessional lateral moraine. The river floodplain and terraces, as well as fans built by tributary streams occupy the valley floor. A prominent set of moraines in the middle reaches of the Macaulay valley ($\sim$1020 m above sea level (a.s.l.)), informally referred to here as the 'mid-Macaulay moraines', are in a position intermediate between LGM moraines down-valley, and modern glaciers and late-Holocene moraines farther up-valley. The mid-Macaulay moraines have previously been assessed as early Holocene in age (e.g., McSaveney and Whitehouse, 1989).

2.2. Previous work on the mid-Macaulay moraines

A buried organic horizon exposed in the western bank of the Macaulay River near the down-valley end of the mid-Macaulay moraines has been a subject of scientific interest for several decades. In 1963, A.C. Beck first described the buried organics and collected a sample of wood (NZ-548) that was subsequently dated using ^{14}C (Grant-Taylor and Rafter, 1971; NZ-548, 8460 $\pm$ 120 ^{14}C yr BP). The stratigraphy was interpreted as 'peat on fan debris and overlain by moraine'. In response to the publication of this date and its geologic interpretation, Burrows (1972) drew attention to the unsorted bouldery deposit that overlies the organic horizon, and the hummocky, boulder-strewn landform developed on this deposit (boulder field in Figs. 1 and 2). Burrows considered that the deposit lacks the fine silt matrix that he regarded as typical of basal till, and noted that the boulder field has a faintly expressed arrangement of ridges that could be interpreted as radiating out from the adjacent northwestern side of the valley; he preferred the interpretation that the deposit is landslide debris. Burrows also noted his impression in the field that the landslide terrain, at its northern margin, laps onto morainal landforms and is therefore younger than the moraines. Beck (1972) endorsed Burrows' reinterpretation of the deposit, and concurred that the ^{14}C date represents a minimum age for the mid-Macaulay moraines.

McSaveney and Whitehouse (1989) reported a visit to the Macaulay valley in 1980 during which they found that river erosion had refreshed the riverbank exposures. They described and discussed the stratigraphic exposures and adjacent landforms, and presented a radiocarbon date (NZ-6473, 8690 $\pm$ 120 ^{14}C yr BP) of wood collected from buried soil about 80 m upstream of the original sample site. McSaveney and Whitehouse (1989) agreed with Burrows' (1972) overall interpretation of the locality, including the general nature of the mid-Macaulay moraines, but disputed the genesis of the deposit (diamicton) overlying the buried soil. They considered that the diamicton lacks characteristic features diagnostic of rapidly emplaced landslide ('rock avalanche') debris, and therefore concluded that the diamicton is till, emplaced in part by subglacial processes (basal till) and in part by passive ice downwasting (ablation till). They noted that they could not discount an alternative interpretation that the diamicton was emplaced by two debris-flow events, the earlier of which deposited the material they interpreted as basal till, and the latter depositing the material regarded as ablation till.

Please cite this article in press as: Putnam, A.E., et al., In situ cosmogenic ^{10}Be production-rate calibration from the Southern Alps, New Zealand, Quaternary Geochronology (2010), doi:10.1016/j.quageo.2009.12.001

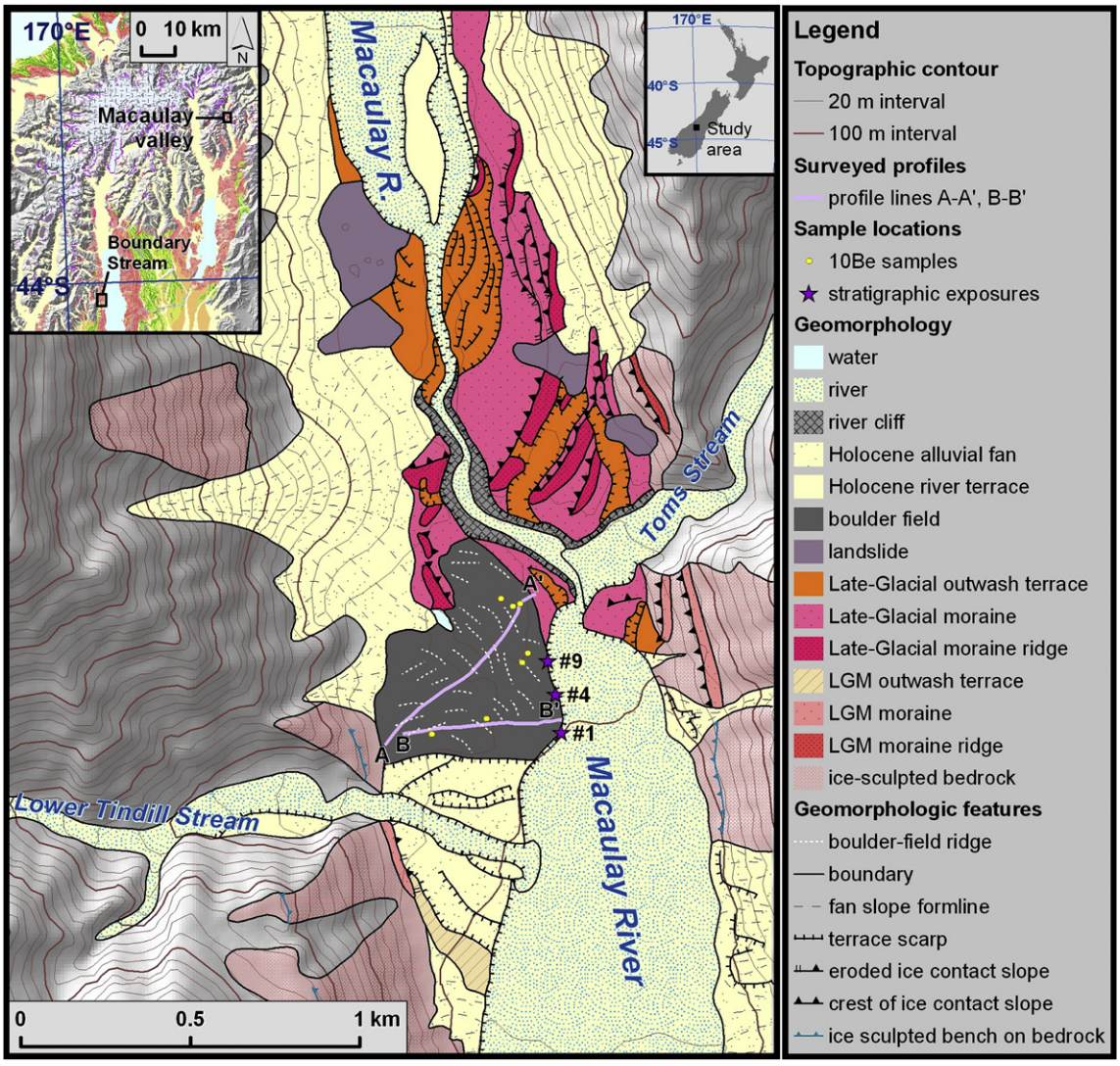

Fig. 1. Geomorphic map of the Macaulay valley study area. Regional location maps and legend are inset. ^{14}C samples were collected from stratigraphic exposure #1.

The most diagnostic morphologic evidence for morainal origin stated by McSaveney and Whitehouse (1989) is that the topographic surface of the deposit slopes down-valley from the mid-Macaulay moraines. On this basis, they expressed confidence that the diamicton was emplaced from that direction, either directly by ice or by glaciogenic debris flows.

2.3. Additional observations and re-assessment of the Macaulay boulder field

We visited the site in January 2008 to evaluate its potential as a ^{10}Be production-rate calibration site. The boulder field is about 500 m across (Figs. 1 and 2). It lies at 43.58°S, 170.61°W, immediately west of the Macaulay River and north of Lower Tindill Stream, and is just over 1000 m above sea level (a.s.l.). The boulder field contains many scattered large, subangular boulders of hard, quartzofeldspathic sandstone (hereafter called greywacke), thoroughly embedded in the ground (Figs. 2 and 3). The ground surface is hummocky with many discontinuous narrow ridges as much as about 3-m high (Fig. 3); a representation of these ridges is mapped in Fig. 1. Erosion by the Macaulay River has produced discontinuous exposures of deposits beneath the boulder field, variably obscured by colluvium and vegetation. The exposures are generally not as fresh or as extensive as those described by McSaveney and Whitehouse (1989). Examination of the landforms and deposits satisfied us of their suitability for calibration purposes. Samples were collected from the boulder field for ^{10}Be measurements (Fig. 3), while the buried soil was sampled for ^{14}C dating (Fig. 4), at approximately the same location as Beck's original sample site.

On a subsequent visit in February 2009, we undertook further examination and mapping of the deposits and landforms, and carried out high-precision surveys of the sample sites and key topographic features using a Trimble ProXH GPS receiver. Both these visits affirmed, in our opinion, the validity of previously reported work. However, we made three additional observations that bear on the origin of the diamicton.

The first is that the boulder field has a greater altitudinal extent than was indicated by McSaveney and Whitehouse (1989). Close to the Macaulay River the boulder field does indeed slope up-valley toward the mid-Macaulay moraines, but also slopes up, to a greater extent, toward the valley of Lower Tindill Stream (Figs. 1, 2 and 5). The second observation is that the boulder field area has a diffuse arrangement of discontinuous narrow ridges (Figs. 1 and 2; also see Fig. 5). The ridge axes are approximately transverse to the mouth of

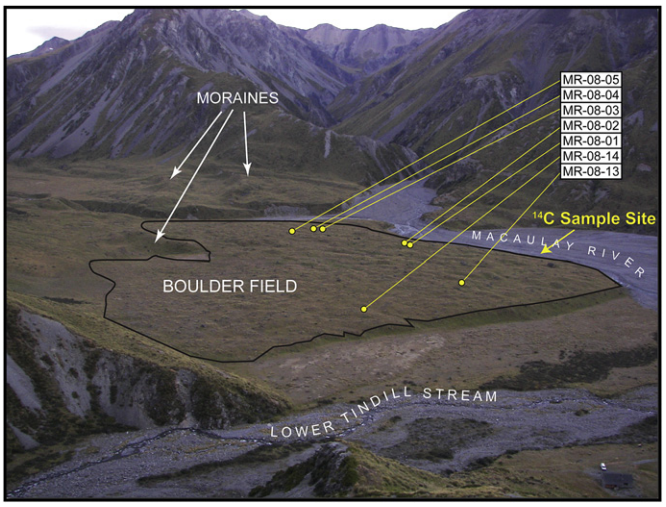

Fig. 2. View northeast across the Macaulay valley study area. The boulder field is outlined in black, with the mid-Macaulay moraines beyond and sediment fans at far left. Fan terraces of Lower Tindill Stream flank the active streambed at lower center to bottom left, where the vehicle and hut illustrate scale. The valley of Toms Stream lies in center distance. We interpret the boulder field to be a product of a debris flow that issued from the valley of Lower Tindill Stream and spread out over a pre-existing fan of this stream as well as over adjacent moraines or outwash terraces of the mid-Macaulay moraine complex. We attribute the position of the boulder field out to the northern side of the Lower Tindill fan as having resulted from the northeastward deflection of the debris flow by the prominent rock bluff in the center foreground.

Lower Tindill Stream valley; they do not have a pattern of trends that are easy to reconcile with ice margin positions of an expanded Macaulay valley glacier. The third observation is that the stems protruding from the buried soil have long axes that are clustered on an approximately east–west trend (sites #1, #4 and #9; Figs. 1, 4, and 6). If we surmise that the woody material represents a shrubland that was flattened during emplacement of the overlying diamicton, that the wood long axes correspond to an azimuth of flow, then the diamicton was emplaced from the either the east or west.

These observations lead us to adopt McSaveney and Whitehouse's (1989) alternative explanation that the diamicton, and its boulder field topography, is the result of a large debris flow. In their explanation of the debris-flow scenario, they identified a finer-grained, discontinuous diamicton as representing an earlier debris flow. The median age of their ^{14}C sample obtained from wood embedded at the base of that diamicton is 230 ^{14}C years older than that of the Beck's sample, which was collected from beneath the coarser-grained diamicton. While noting that the ages are indistinguishable within error, they suggested an age difference of several centuries between the hypothesized debris-flow events. As presented below, our ^{14}C sampling, close to Beck's sample site and thus beneath the coarse-grained diamicton, returned ages indistinguishable from that obtained by McSaveney and Whitehouse (1989). We suggest that the finer-grained diamicton may represent an initial pulse of material deposited at the leading edge of a fast-moving debris flow and that it may be only a matter of seconds older than the overlying coarse-grained diamicton. Alternatively, the finer-grained diamicton may relate to an earlier debris flow; the ^{14}C age error ranges imply that if so, it preceded the emplacement of the coarse-grained diamicton by no more than about two centuries.

In summary, morphologic and topographic evidence lead us to interpret the Macaulay boulder field as a product of a large debris flow that issued from the valley of Lower Tindill Stream. Topographic profiles (Fig. 5) reveal an eastward slope on most of the boulder field area that is similar to the slope of the alluvial fan of

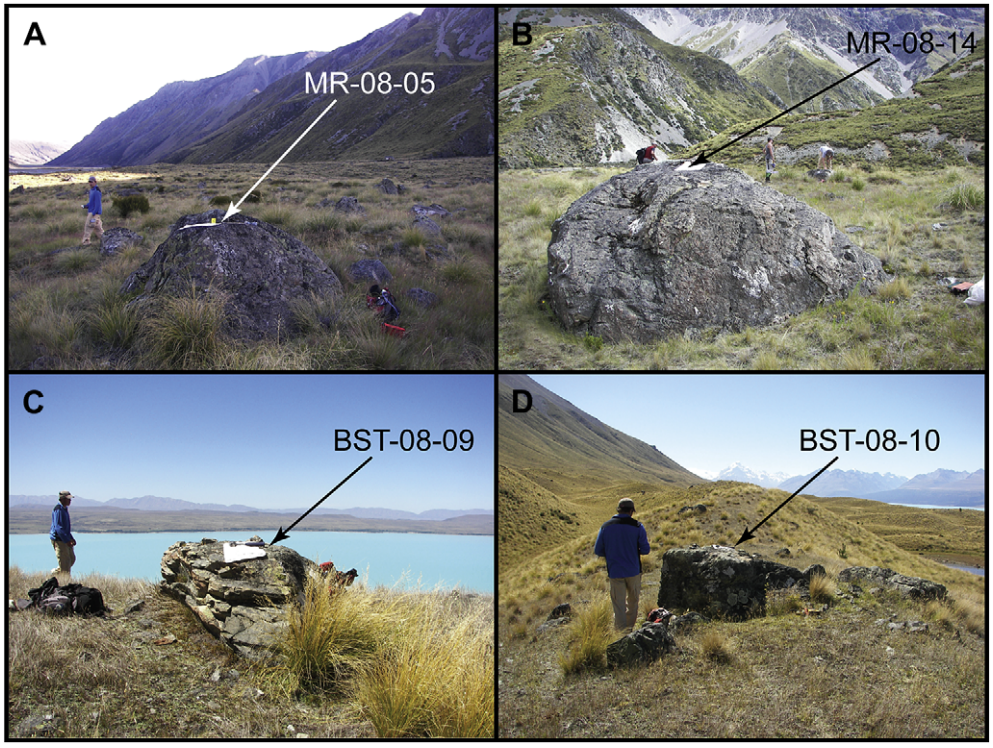

Fig. 3. Examples of boulders in the Macaulay boulder field (A and B) and Boundary Stream moraines (C and D) selected for sampling for ^{10}Be measurements. Sample sites are arrowed. The person in blue (S. Kelley) is 1.7 m tall. Photo A looks south with the lower reaches of the Macaulay valley and the western flank of the Sibbald Range in the background. In photo B, the view is southwest toward the mouth of the Lower Tindill Stream valley. In Photo C the view is to the northeast, with the Lake Pukaki basin and left-lateral moraine system visible in the background. Photo D looks to the north, with Aoraki/Mt. Cook the center distance. Sample bag (46 × 28 cm) on the boulder provides a scale (For interpretation of the references to colour in this figure legend, the reader is referred to the web version of this article.)

Please cite this article in press as: Putnam, A.E., et al., In situ cosmogenic ^{10}Be production-rate calibration from the Southern Alps, New Zealand, Quaternary Geochronology (2010), doi:10.1016/j.quageo.2009.12.001

Fig. 4. Stratigraphic section and photographs of the Macaulay ^{14}C sample site (see Figs. 1 and 2). Stratigraphic units (S) are organic topsoil (S1), yellow–brown silt loess (S2), bouldery silty gravel diamicton (S3), buried soil comprising organic silt-clay with wood and leaves (S4) and sandy pebble-gravel alluvium (S5). Photo to the right shows shrub stems and branches protruding from the buried soil. Wood from similar stems or branches, sampled in 1963 at about this location, provided the original ^{14}C date (Grant-Taylor and Rafter, 1971). (For interpretation of the references to colour in this figure legend, the reader is referred to the web version of this article.)

Lower Tindill Stream, and that in the northern half of profile A–A′, the slope reverses and rises to the north. We take this to indicate that the debris flow spread down over a pre-existing fan of Lower Tindill Stream and then ran out and up onto adjacent moraines or outwash terraces of the mid-Macaulay moraine complex. We attribute the position of the boulder field out to the northern side of the Lower Tindill fan as having resulted from the northeastward deflection of the debris flow by a prominent bedrock bluff on the southern side of the Lower Tindill valley mouth (Figs. 1 and 2). To account for the large extent of the deposit and the debris flow having had sufficient velocity and fluidity to spread uphill to the north, we speculate that a sizeable rock avalanche may have come down in the middle reaches of Lower Tindill Stream, blocking the stream and creating a lake. We hypothesize that a rapid failure of a landslide dam formed the debris flow, which in transit entrained substantial volumes of alluvial sediment from the Lower Tindill valley floor. This could account for the variety of greywacke and argillite lithologies in clasts in the deposit, the presence of clast angularities ranging from angular to round, and the bruising and striation of some clasts that could have occurred in transit within the flow. We consider that this explanation is compatible with all observations reported by Burrows (1972), Beck (1972) and McSaveney and Whitehouse (1989).

Thus, our main conclusion for the geomorphic component of this study is that the Macaulay boulder field is the topographic surface of a large debris-flow deposit that was emplaced in a single relatively rapid event. The debris flow overwhelmed a shrubland growing on a fan-moraine-terrace landscape, killing and burying vegetation at approximately the same moment as the surface boulders began their exposure to the incoming cosmic-ray flux, i.e., within ^{10}Be and ^{14}C dating uncertainties. This site affords a stratigraphic and geomorphic context well suited for ^{10}Be production-rate calibration against an independent radiocarbon chronology.

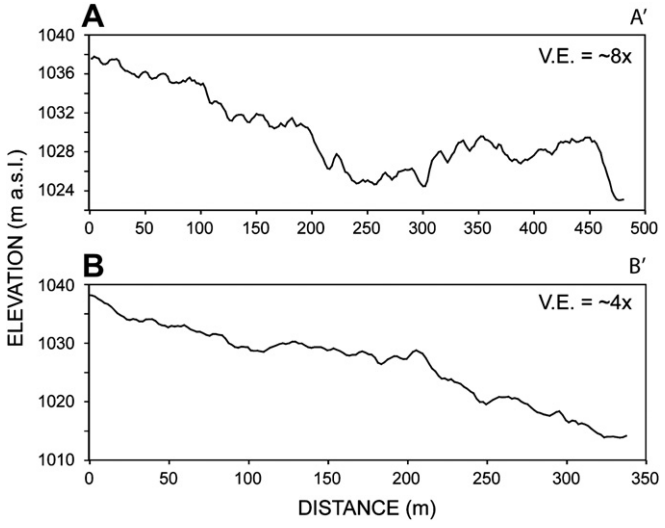

Fig. 5. Topographic profiles of the Macaulay boulder field; see Fig. 1 for profile locations. Profiles were measured with differential GPS. Elevation uncertainties (1σ) range from 0.1 to 0.6 m. V.E. is vertical exaggeration.

2.4. The boundary stream tarn (BST) moraines

About 60 km southwest of Macaulay valley, the LGM right-lateral moraines of the Lake Pukaki basin north of Boundary Stream contain many small ponds and closed depressions of moraine-dammed or glacio-karst origin. The ponds are rain-fed and most are seasonally dry, although one of the largest (Boundary Stream tarn (BST); ~850 m a.s.l.) is perennially water-filled (Figs. 1 and 7). Vandergoes et al. (2008) described the sediments from this pond, based on two composite cores, and developed a detailed radiocarbon chronology of sedimentation, the results of which are reproduced below in Section 4.2. Scattered boulders between 50 and 100 cm in height are embedded in many of the adjacent moraine ridges (Fig. 3).

The geomorphology of the BST moraines is shown in Fig. 7. A prominent lateral moraine ridge west (i.e., outboard) of BST is interpreted to have formed at the culmination of the last major advance of the Pukaki Glacier during the LGM. Moraines inboard of BST occur as a narrow band of hummocky, discontinuous ridges at the edge of a major moraine wall. This moraine wall represents the rapid glacier retreat that occurred at the onset of the last glacial termination (Schaefer et al., 2006). In this case, radiocarbon analyses of the BST sediments by Vandergoes et al. (2008) afford a minimum limit on the date that the outboard bounding moraines were abandoned by the Pukaki Glacier. Boulders embedded in the moraines outboard of BST must have commenced their exposure to the cosmic-ray flux prior to the deposition of the oldest BST sediments. Thus, radiocarbon dates of BST sediments afford minimum ages for moraines immediately adjacent to and outboard of BST.

Please cite this article in press as: Putnam, A.E., et al., In situ cosmogenic ^{10}Be production-rate calibration from the Southern Alps, New Zealand, Quaternary Geochronology (2010), doi:10.1016/j.quageo.2009.12.001

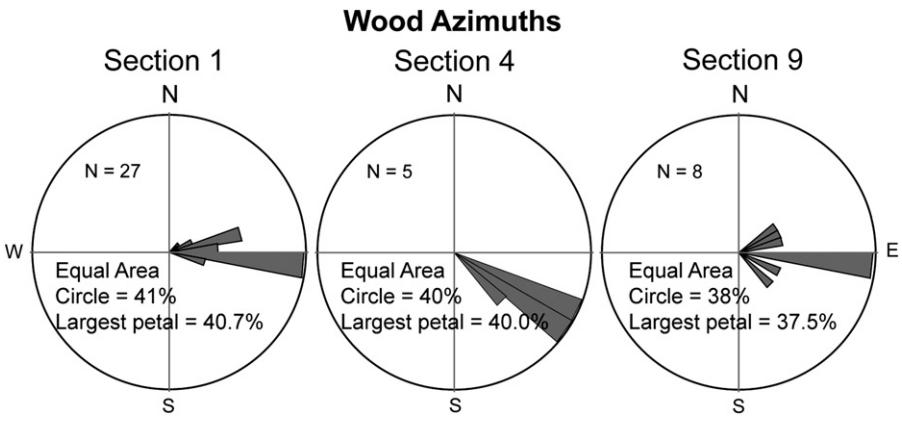

Fig. 6. Rose diagrams showing azimuths of wood long axes in buried soil at Macaulay sites #1, #4 and #9 (see Fig. 1). At each exposure, we measured the azimuths of all exposed wood stems that were 1 cm or more in diameter.

This morpho-stratigraphic relationship allows us to test the production rates derived from the Macaulay site, as well as other available production rates.

3. Methods

3.1. Radiocarbon dating of the Macaulay valley debris flow

We selected ten samples for radiocarbon dating from the soil horizon that is buried directly beneath the debris-flow-derived diamicton. Six samples of *Phyllocladus* sp. leaves and one sample of *Podocarpus* sp. leaves were collected from a concentration of leaves in the uppermost part of the buried soil, while the other samples consisted of three small twigs, and one piece of bark from a protruding branch (Fig. 8). The samples were transported to GNS Science in Lower Hutt, New Zealand, where they were rinsed with deionized water, scrubbed of any enclosing sediment, and dried at 50 °C. We sent all samples to the Woods Hole Oceanographic Institution (WHOI) for ^{14}C analysis at the National Ocean Sciences Accelerator Mass Spectrometry facility (NOSAMS), where samples were processed using the 'organic combustion' method described at the WHOI NOSAMS website (http://www.nosams.whoi.edu/clients/processes.html#organic_combustion).

3.2. Radiocarbon dating of the BST sediments

Vandergoes et al. (2008) described radiocarbon sampling, AMS analyses and the resulting age model derived from seventeen

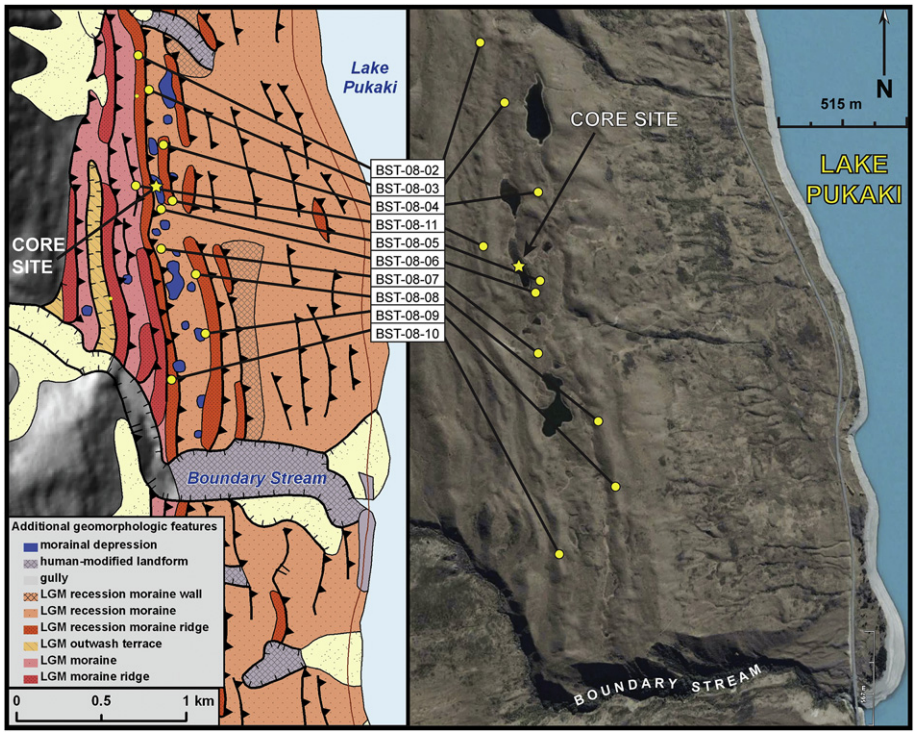

Fig. 7. The Boundary Stream tarn moraines. Left panel shows a glacial geomorphic map of the Boundary Stream area. The main geomorphologic features are included in the Fig. 1 legend, with additional geomorphic features in the legend inset. Yellow dots show ^{10}Be sample sites, with names in white boxes. The yellow star marks the site of the cores described by Vandergoes et al. (2008). Right panel is a Google Earth satellite image of the moraine complex (captured 04 May 2006), showing general landform textures and sample locations. (For interpretation of the references to colour in this figure legend, the reader is referred to the web version of this article.)

Please cite this article in press as: Putnam, A.E., et al., In situ cosmogenic ^{10}Be production-rate calibration from the Southern Alps, New Zealand, Quaternary Geochronology (2010), doi:10.1016/j.quageo.2009.12.001

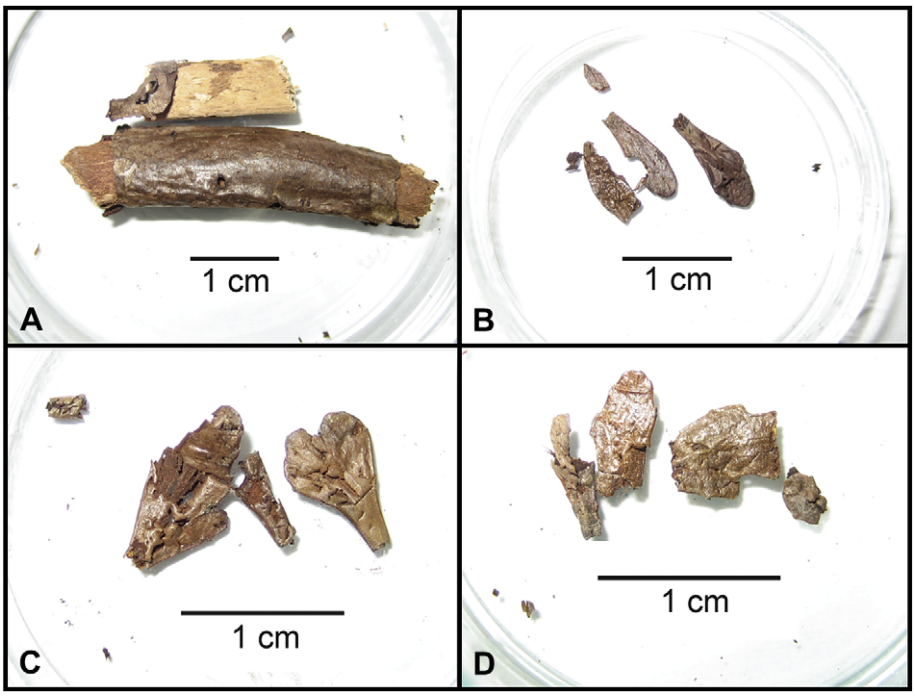

Fig. 8. Examples of plant macrofossils from the Macaulay sample site (see Figs. 1 and 4) selected for radiocarbon dating. Panel A shows wood twig (top) and wood with bark (bottom) that yield ages of 8630 ± 55 ^{14}C yrs BP (OS-68140) and 8760 ± 40 ^{14}C yrs BP (OS-68141), respectively. Panels B–D show *Phyllocladus* sp. leaves that give ages of 8820 ± 50 ^{14}C yrs BP (OS-68211), 8750 ± 45 ^{14}C yrs BP (OS-68208), and 8800 ± 40 ^{14}C yrs BP (OS-68065), respectively.

samples (including replicates) collected from 1-cm-thick slices of bulk sediment. The deepest samples came from within the upper 10 cm of a stiff, gray, diamicton at the base of the pond sediments. The rest of the samples came from the brown organic silt that constitutes most of the core. Samples were analyzed at the WHOI NOSAMS facility using the 'organic combustion' method.

3.3. ^{10}Be surface-exposure dating

From the Macaulay debris-flow deposit we sampled fourteen boulders and processed seven samples for ^{10}Be measurement. We collected and processed eleven samples from boulders located on ridge crests of the Boundary Stream tarn moraines. Samples chosen for processing came from boulders at least 60 cm high and at least 100 cm across (Fig. 3). We selected boulders with broad, low-relief tops, which did not show any indications of surface pitting, exfoliation, fracturing, or rainwater pooling. No soil erosion or post-depositional landform degradation is apparent near the sampled boulders, and all boulders sampled are located away from steep valley walls, talus fans, and riverbanks. In the case of the Macaulay valley debris-flow deposit, sampled boulders are away from moraines.

Samples were collected with hammer and chisel. For very hard boulders, we used the drill-and-blast method of Kelly (2003). At each sample site we measured boulder dimensions and photographed the boulder and sample surface from several different angles. To determine topographic shielding, we measured the azimuthal elevations of the surrounding landscape at each sample locale using compass and clinometer, and recorded the strike and dip of the sampled surface of each boulder. Sample locations and altitudes were measured using a Trimble ProXH GPS system relative to the WGS 1984 datum, and all measurements were subsequently corrected differentially using continuous data collected by the Mt. John Observatory base station (MTJO; latitude: −43.985706, longitude: 170.464943, height above ellipsoid: 1043.660 m; height above mean sea level relative to the tide-gauge data at Lyttelton, New Zealand: 1037.46 m). The MTJO base station is located 47 km south of the Macaulay valley site, and 28 km east of the Boundary Stream tarn moraines. Post-processed horizontal and elevational uncertainties (1σ) ranged from 0.1 to 0.4 m, and 0.1 to 0.6 m, respectively, for all sample sites. Elevation data were converted to meters above mean sea level. We tested the accuracy of the GPS elevation data by measuring the elevation of a survey marker located on the western shore of Lake Pukaki, just north of Boundary Stream (trigonometrical station 'B2T1-C' (Pukaki West SD); 544.6 ± 1.0 m a.s.l.). We determined a corrected GPS elevation of 545.2 ± 0.2 m a.s.l. (1σ), showing agreement to within 1 m of the reported survey mark elevation.

All samples were processed for ^{10}Be analysis at the Lamont-Doherty Earth Observatory (LDEO) cosmogenic nuclide laboratory, following the protocol available at the laboratory website (http://www.ldeo.columbia.edu/tcn), which is modified from Licciardi (2000) and the procedure developed by the University of Washington cosmogenic group (http://depts.washington.edu/cosmolab/chem.html). Sample ^{10}Be/^{9}Be ratios were measured relative to the 07KNSTD3110 standard (^{10}Be/^{9}Be = 2.85 × 10^{-12}; Nishiizumi et al., 2007), and corrected for background ^{10}Be/^{9}Be given by the procedural blanks (all were less than 1 × 10^{-15}), residual boron contamination, and machine background (<1.3% in all cases).

3.4. Production-rate and exposure-age calculations

We followed the methods and terms described in Balco et al. (2009) for our production-rate calculations, and used the exposure-age calculation methods incorporated in the CRONUS-Earth online exposure age calculator, Version 2.2 (Balco et al., 2008). Mean sea level air pressure (SLP) and 1000 hPa air temperature were derived from the NCAR World Monthly Surface Station Climatology dataset implemented in the CRONUS calculator (http://www.cdc.noaa.gov/ncep-reanalysis). SLP data averaged over the period AD 1854–2007 at nearby climate stations, obtained from the New Zealand National

Institute of Water and Atmosphere National Climate Database (NIWA CliDB; http://www.niwa.cri.nz/services/clidb), compares well with values obtained from the NCAR dataset (NCAR SLP value = ~1013 mb, NIWA SLP value = 1012.7 mb).

We used azimuthal elevation data to calculate the effect of topographic shielding on the incoming cosmic-ray flux using the online program developed by Balco et al. (2008). All calculations include a rock sample thickness correction derived from the measured mass-weighted average thickness, using an assumed rock density value of 2.7 g cm^{-3} and neutron attenuation length of 177 g cm^{-2} (Farber et al., 2008). Muon production is determined for each sample using the CRONUS-Earth calculator, which implements the muon production rates outlined in Heisinger et al. (2002a,b), and the altitudinal scaling method of Boezio et al. (2000). Muon production rates derived in this manner are independent of all nucleon scaling schemes.

We deemed that corrections for boulder surface erosion, snow cover, and time-dependent changes in air pressure were not necessary. In general, surface erosion rates on the dry, east side of the Southern Alps, are low (e.g., Jackson et al., 2002; Youngson et al., 2005). Indurated greywacke sandstone is resistant to granular disintegration (e.g., Birkeland, 1982), so we follow Schaefer et al. (2006, 2009) in assuming the effects of erosion to be negligible over the time-scales discussed here. Although spalling is apparent on the sides of some boulders, top surfaces show no visual indication of material lost at the sample sites. Winter snow cover is ephemeral at the Macaulay and BST sites, with a 1-m snowfall being an exceptional event that typically melts away within a few weeks. Wind also tends to remove snow from salient boulder surfaces. We assume that atmospheric pressure has remained stable during the Holocene. The results of Staiger et al. (2007) imply that atmospheric conditions during the LGM would have resulted in only slight changes in cosmogenic nuclide production rates (<2% lower) in New Zealand. The slightly lower LGM production rate due to higher LGM SLP, when integrated over the duration of exposure of the BST moraines, has a negligible effect on the results presented below, and is therefore not incorporated into age calculations.

All calculations are comparable with those of Balco et al. (2008, 2009). To calculate 'best-fit' production-rate values, we used the least-squares method described by Balco et al. (2009), which chooses the ^{10}Be reference production rate that minimizes the misfit between the calculated and independently determined exposure age for the calibration site. As described above, muonogenic ^{10}Be production is scaled and determined by the CRONUS-Earth calculator (Balco et al., 2008). Therefore, production rates presented and discussed below are for production by spallation only (after Balco et al., 2008, 2009). We adopt the abbreviations of Balco et al. (2008) that describe the various spallogenic nucleon scaling methods included in the CRONUS-Earth online calculator: 'St' = Stone (2000) following Lal (1991); 'Du' = Dunai (2001), 'De' = Desilets et al. (2006), 'Li' = Lifton et al. (2005), and 'Lm' = the time-dependent adaptation of Lal (1991).

3.5. Assessment of landscape uplift and its potential impacts on local production rates

Another important consideration is whether tectonic and/or glacioisostatic uplift has influenced the production rate of ^{10}Be at the Macaulay and BST sites. Uplift raises a land surface into progressively higher altitudes and thus progressively lower atmospheric pressures and greater cosmic-ray fluxes. Therefore, a production rate derived from a landform that has been rising underestimates the nuclide production at its present elevation.

Late Quaternary tectonic uplift rates in the Southern Alps are best constrained in the west, where late Pleistocene and Holocene deposits and landforms have been offset at the Alpine Fault (AF). Several localities provide constraint on strike-slip or dip-slip rates but only one locality in the vicinity of the central Southern Alps, Paringa River, provides robust constraint on the uplift rate, by virtue of marine deposits in an infilled post-glacial fjord that reached inland of the AF. Although slightly to the southwest of the highest part of the Southern Alps, the latest Pleistocene to Holocene uplift rate at Paringa, after removal of the effects of localized anticlinal folding, is 8 ± 1 mm yr^{-1} (Norris and Cooper, 2001). Elsewhere, there are few quantitative direct indicators of long-term uplift, but estimates may be derived from less direct methods.

Geologic mapping provides a picture of the evolution of the Southern Alps that bears on uplift patterns. In the early to middle Cenozoic, progressive exhumation and erosion of the Mesozoic greywacke and schist basement rock was succeeded unconformably by deposition of a marginal-marine to marine regionally transgressive sedimentary sheet. Inception of the present plate boundary through New Zealand in the earliest Miocene led to regression and increasingly non-marine sedimentation. Development of a more convergent plate vector in the Late Miocene-Early Pliocene led to formation of the Southern Alps, illustrated stratigraphically by an influx of greywacke or schist conglomerates to basins west and east of the mountain chain. Deformation was dominated by movement on the Alpine Fault, but also characterized to the east by evolution of a fault-controlled basin and range province (Cox and Barrell, 2007). Dissected ranges of uplifted basement rock versus the more subdued basin landscape developed on Cenozoic sedimentary rocks or Quaternary deposits are well expressed in the topography (Fig. 9). Carbonaceous beds in the Miocene–Pliocene sedimentary rocks are of lignite grade, indicating that they have not been deeply buried. Preservation of Pliocene and older sedimentary rocks qualitatively constrains the amounts of uplift and erosion that can have occurred during growth of the Southern Alps.

Thermochronometry provides constraints on rates of rock exhumation using techniques such as fission-track (FT) analysis. A recent synthesis of thermochronometric studies (Herman et al., 2009) builds on earlier work by Tippett and Kamp (1993), Batt et al. (2000) and Little et al. (2005), as well as incorporating geologic and geophysical constraints. In the greywacke and schist basement rocks of central Southern Alps, the apatite fission track (aFT) thermochronometer, which indicates time elapsed since the rock cooled below ~110 °C, shows a general change about 30 km southeast of the AF trace, with very young (Late Pliocene to Pleistocene) ages to the northwest, and progressively older ages, Eocene to Pliocene, to the southeast (Fig. 9). Ages are consistently Eocene or older beyond about 40 km southeast of the AF trace. These findings are commensurate with the preservation of Miocene to Pliocene sedimentary rocks in basins within the region where pre-Pliocene aFT ages have been obtained from the stratigraphically underlying basement rocks. The aFT ages reinforce the conclusion that on the eastern flank of the Southern Alps, away from the crest of uplifted fault blocks, total amounts of post-Pliocene regional uplift and erosion have not been great.

In the Mackenzie Basin, uplift on the Ostler and Irishman Creek reverse fault blocks is concentrated over the hanging walls close to the surface traces, and diminishes rapidly towards the down-dip direction, indicating a listric fault geometry at depth (Amos et al., 2007). This suggests that while fault block displacements influence the uplift pattern (Herman et al., 2009), for example with late Quaternary vertical uplift rates of the order of 1 mm yr^{-1} at the crest of the hanging wall of the Ostler Fault, most of the uplift is localized (Amos et al., 2007). Neither the Macaulay nor the BST sites lie on the hanging wall of any known late Quaternary active faults.

Herman et al. (2009) accounted for the geologic and thermochronologic constraints by modeling the AF as having a moderate

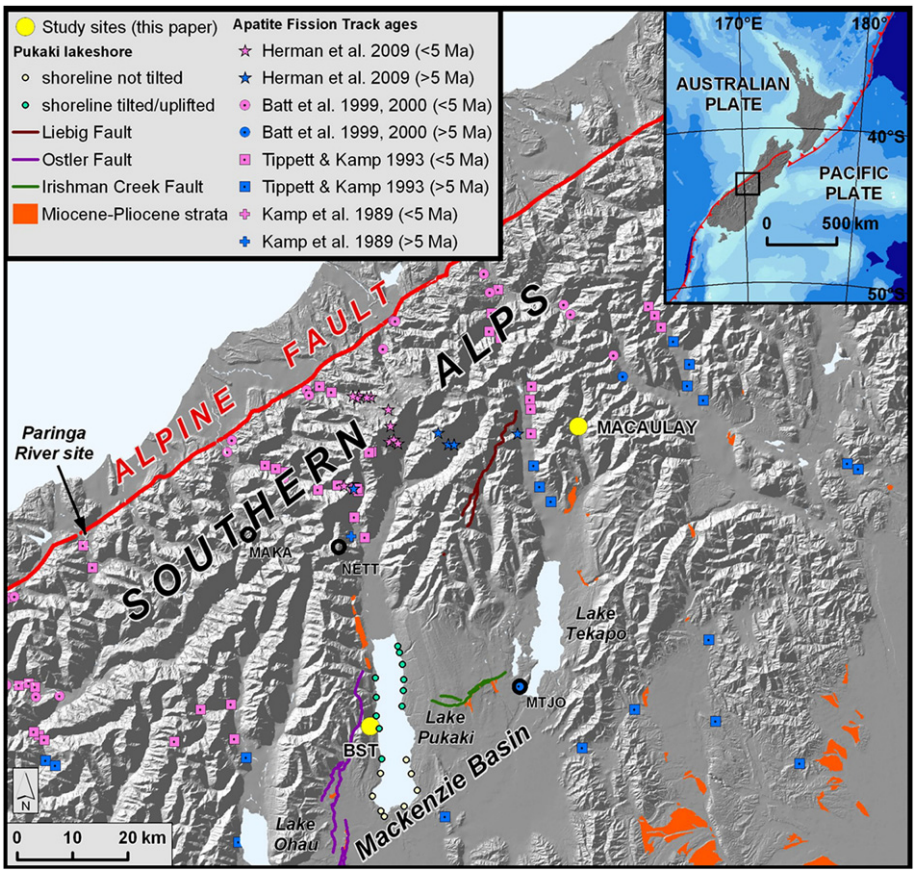

Fig. 9. Constraints on uplift of the Southern Alps include radiocarbon-dated deposits at Paringa River (Norris and Cooper, 2001), apatite fission track (aFT) ages (Kamp et al., 1989; Tippett and Kamp, 1993; Batt et al., 1999, 2000; Herman et al., 2009), late Cenozoic stratigraphy and faulting (Cox and Barrell, 2007), and post-LGM lake-shoreline deformation (this paper). Black circles denote the locations of continuous GPS stations MAKA, NETT and MTJO (Beavan et al., 2004, 2007). The aFT ages are subdivided into those of reported median age greater than 5 million year (Ma) versus those younger than 5 Ma, which have been exhumed from closure temperatures during formation of the Southern Alps. The inset illustrates the plate tectonic setting. The plate boundary through South Island is marked by the Alpine Fault, which passes southward to the Puysegur subduction zone, while the Hikurangi subduction zone lies east of North Island. We plot the data of Batt et al. (2000) using the geographic coordinates given in Table 1 that paper.

southeasterly dip in the upper crust (nominally 45–60°), passing onto a gently dipping ramp (nominally 10°) in the mid- to lower crust, and then merging onto a flat decollement. Of several alternative geometries of this conceptual model, the best fit with thermochronometric measurements comprised a high rate of uplift extending ~22 km southeast of the AF trace, associated with a moderately dipping fault ramp, succeeded to the southeast by a zone of much slower uplift extending out to about 90–100 km southeast of the AF trace associated with a gently dipping ramp. This kinematic model allows quantitative estimation of long-term rates of tectonic uplift in the general area of our study sites. Plate-movement vector estimates imply a convergence vector of ~9 mm yr^{-1} perpendicular to the AF. Taking the fault ramp dip estimates at face value, this implies an average uplift rate of at least 9 mm yr^{-1} over the moderately dipping ramp, whose effect is suggested to extend as much as ~22 km southeast of the AF trace, but only 1.6 mm yr^{-1} uplift over the gently dipping ramp. As our study sites lie 38 km (Macaulay) and 60 km (Boundary Stream) southeast of the AF trace, this implies a tectonic uplift rate of approximately 1.6 mm yr^{-1} at our study sites.

While the Herman et al. (2009) model is based primarily on long-term (>10^5 yr) rock exhumation patterns, and thus provides proxy constraints on long-term uplift rates, is it applicable to the shorter time spans considered in this paper? We examine this question by presenting geomorphic evidence from post-LGM lake shorelines (10^3–10^4-yr timeframe) at Lake Pukaki adjacent to the Boundary Stream site, and by evaluating emerging results from GPS measurements (10^0-yr timeframe).

At Lake Pukaki, high-stand post-LGM lake levels are recorded by well-defined shoreline features (Bunting, 1977) for which we infer an age of approximately 16 033 ± 750 cal yr based on radiocarbon dating of LGM ice-retreat landforms (Moar, 1980). Although the lake was raised in 1979 for hydro-electric water storage, drowning the post-LGM shorelines, aerial photographs, topographic contour maps and geotechnical reports that pre-date the lake rise have allowed us to map the post-LGM shoreline. The shoreline is at a constant altitude beyond 65 km southeast of the AF trace, but progressively increases in height to the northwest of the 65 km mark (Fig. 9). Assuming that the 65 km mark represents a zero isobase for Southern Alps uplift in the Lake Pukaki area, the shoreline is about 8 m higher adjacent to Boundary Stream, which implies an average post-glacial uplift rate of 0.5 mm yr^{-1}. The northwestern limit of the preserved shoreline, ~50 km southeast of the AF trace, is about 14 m higher than at the presumed zero isobase, and implies an average post-glacial uplift rate of 0.9 mm yr^{-1}. The well-defined change in shoreline height, and its steady rise, may confidently be attributed to tectonic processes because it occurs within the area glaciated during the LGM and thus is unlikely to reflect a glacioisostatic response.

Since AD2000, continuous and semi-continuous GPS measurements have been collected from stations that transect the central Southern Alps (Beavan et al., 2004, 2007). This transect is oriented

northwest-southeast, broadly perpendicular to the AF trace, and passes between the Macaulay and BST areas (Fig. 9). Results of October 2005 (the most recent published compilation; Beavan et al., 2007), show the maximum average rate of vertical rise on this transect is 5.4 mm yr^{-1}, based on the upper limit of the 95% confidence interval for data recorded at 'MAKA' station, 16 km southeast of the AF. The 'NETT' station, located 29 km southeast of the AF trace, has recorded a vertical rise of 1.8 ± 1.0 mm/yr (Beavan et al., 2004, 2007). The Mount John Observatory station ('MTJO'), 68 km southeast of the AF trace, has recorded no significant vertical rise (Beavan et al., 2004, 2007). A limitation of these ultra short-term GPS data is that they may include transient elastic strains that may or may not resolve into permanent strain on a geomorphic timescale (e.g. $\geq 10^2$ yr). Furthermore the GPS data underestimate uplift rates close to the AF, due to the fault currently being locked in the upper to middle crust, pending the next large-scale accrual of permanent strain expected in association with the next ground-surface rupturing AF earthquake. Although these GPS estimates may not adequately represent overall Holocene uplift rates, they are broadly compatible with the longer-term indicators of uplift.

In conclusion, uplift indications provided by post-LGM lake shorelines as well as contemporary precise GPS data appear to be compatible with the much longer-term perspective provided by geology and thermochronometry. Given the lack of contemporary uplift at Mt John, we tentatively infer that the untilted Lake Pukaki shorelines more than 65 km southeast of the AF do indeed represent a local zero isobase for Southern Alps uplift. The Pukaki shoreline data suggest that some refinements could be made to the kinematic models of Herman et al. (2009), in that the Late Quaternary uplift of the Southern Alps commences about 65 km southeast of the AF trace, rather than at 90–100 km as in their preferred model, and the fact that the shoreline is tilted indicates a progressive increase in uplift rate more suggestive of a progressive increase in fault dip, rather than a simple flat-to-ramp transition. Despite this, the broad match between the Herman et al. (2009) models and thermochronologic data supports the notion of lesser uplift rates to the southeast and greater rates to the northwest. Our preferred estimate of tectonic uplift at the Macaulay site is 2 ± 1 mm yr^{-1} commensurate with the contemporary rate at the NETT GPS site, the latest Pleistocene-Holocene rate at the northwestern limit of the Pukaki shorelines, and the longer-term rates implied by thermochronometry. We adopt 0.5 ± 0.5 mm yr^{-1} for the BST site, based on the relative heights of lake shorelines and tentatively corroborated by the emerging GPS data.

Therefore, incorporating a nominal 2 mm yr^{-1} uplift rate, integrated linearly over the duration of exposure at the Macaulay debris-flow deposit, yields production-rate values that are 1.03% (St), 1.02% (De), 1.02% (Du), 0.95% (Li), and 1.06% (Lm) greater than when assuming no uplift. As a sensitivity test, choosing maximum uplift rates of 3 and 6 mm yr^{-1} result in 1.29/2.54% (St), 1.27/2.51% (De), 1.28/2.52% (Du), 1.42/2.56% (Li), and 1.57/2.60% (Lm) increases, respectively, in our calculated production-rate values.

Finally, Mathews (1967) provided a quantitative examination of the question of glacioisostatic rebound. Mathews (1967) calculated a maximum post-glacial rebound of about 100 feet ($\sim$30 m) in the Southern Alps. Integrated linearly over the last $\sim$16 000 yr this equates to a maximum uplift rate of 1.5 mm yr^{-1}. Employing a decaying-exponential uplift curve, typical of post-glacial rebound signals (cf. Benn and Evans, 1998), would produce lower integrated uplift values. The lack of contemporary uplift at the MTJO GPS station implies that any such glacioisostatic rebound has finished. We therefore assume that the effect of isostatic rebound on ^{10}Be production at the Macaulay site is probably negligible, since the early Holocene landform was emplaced after most of the isostatic recovery would have taken place following the demise of the large LGM glaciers. As the above estimated uplift corrections are within the range of the time-integrated production-rate uncertainties reported below, and for the sake of consistency with previously published production rates, we follow Balco et al. (2008, 2009) and do not include these uplift effects in our production rate and exposure-age calculations.

4. Results

4.1. ^{10}Be production rates derived from the Macaulay valley

4.1.1. Radiocarbon data

Results from radiocarbon analyses are given in Table 1. We report ^{14}C ages using the conventions described in Stuiver and Polach (1977). Nine of the ten samples yield internally consistent ages that overlap within 1σ, ranging from 8820 ± 50 to 8630 ± 60 ^{14}C yrs. The single exception was the different leaf type, a sample of *Podocarpus* sp., which gave a significantly older age of 9010 ± 50 ^{14}C yrs BP, and is an outlier according to the Grubbs test ($P < 0.02$; Grubbs, 1969), as well as the Chauvenet criterion (Bevington and Robinson, 1992). The reduced dataset excludes the outlier, and yields an arithmetic mean age ($\pm 1\sigma$) of 8750 ± 60 ^{14}C yrs BP, and an error-weighted mean age of 8755 ± 15 ^{14}C yrs BP (Fig. 10).

To determine the calibrated calendrical age of the debris-flow deposit, we used the "R-Combine" component of the OxCal version 4.0.5 program (http://c14.arch.ox.ac.uk/oxcal; Bronk Ramsey, 2007; Bronk Ramsey et al., 2001), which uses a probability density function of the radiocarbon ages to determine the calibrated age range (Fig. 11). The program follows Telford et al. (2004) and uses the weighted average of the radiocarbon age population to develop a single representative age estimate necessary for production-rate determination. This protocol assumes that the radiocarbon ages represent a single population, which is tested by OxCal 4.0.5 using the χ^2 statistical method (Bronk Ramsey et al., 2001). We used the SHCal04 curve (0–11 000 cal yr BP) for calendar-age conversion, which implements the IntCal04 scheme, but accounts for a $\sim$40 ^{14}C-yr offset resulting from a small difference in the atmospheric radiocarbon concentration detected between the hemispheres (McCormac et al., 2004). Ages are expressed as 'years before AD2008' to maintain consistency with surface-exposure years (following Schaefer et al., 2009), which we take to represent years before AD2008, the year in which the Macaulay valley boulders were sampled. We note that this convention also shifts the 'zero age' of the time-dependent scaling models forward by 58 years, since the underlying geomagnetic and solar records are all referenced to AD 1950 as currently implemented. This effectively displaces the

Table 1
Radiocarbon data assayed from buried organic material in the Macaulay valley (site #1 in Fig. 1). Age of OS-68048, shown in italics, is an outlier ($P < 0.02$) according to the Grubbs test (Grubbs, 1969).

^{14}C lab no.	Sample ID	Material dated	δ^{13}C (‰)	^{14}C age $\pm 1\sigma$ (^{14}C yrs BP)
Macaulay Valley				
OS-68048	MC/08/04_A	*Podocarpus* sp. leaves	−27.27	*9010 ± 50*
OS-68065	MC/08/08_A	*Phyllocladus* sp. leaves	−26.13	8800 ± 40
OS-68137	MC/08/14_B	Twig	−25.27	8690 ± 45
OS-68138	MC/08/14_A	Twig	−25.49	8780 ± 45
OS-68139	MC/08/07_A	*Phyllocladus* sp. leaves	−25.07	8750 ± 40
OS-68140	MC/08/01_A	Twig	−25.95	8630 ± 55
OS-68141	MC/08/01_B	Bark	−26.62	8760 ± 40
OS-68208	MC/08/02_A	*Phyllocladus* sp. leaves	−23.91	8750 ± 45
OS-68209	MC/08/09_A	*Phyllocladus* sp. leaves (green)	−28.13	8800 ± 40
OS-68210	MC/08/09_B	*Phyllocladus* sp. leaves	−25.52	8720 ± 45
OS-68211	MC/08/23_A	*Phyllocladus* sp. leaves	−24.38	8820 ± 50

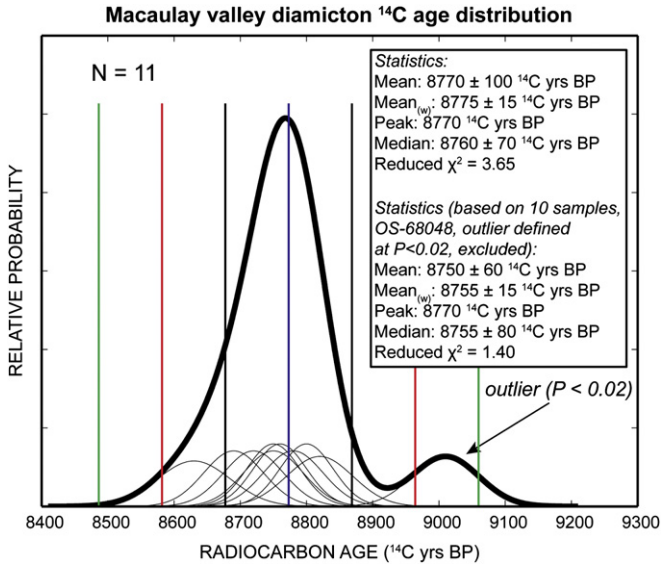

Fig. 10. Probability density plot (i.e., 'camel plot'; G. Balco, personal communication, 2009) showing distribution of radiocarbon ages from the Macaulay valley sample site. Grey curves are Gaussian representations of individual radiocarbon ages, while the black curve shows the summed probability of the total population accompanied by summary statistics. Black, red and green vertical lines mark one, two, and three standard deviations of the whole sample population, respectively, while the blue vertical line denotes the mean value. Sample OS-68048, arrowed, is an outlier ($P < 0.02$), and is excluded from statistical analyses used in calibration calculations (For interpretation of the references to colour in this figure legend, the reader is referred to the web version of this article.).

calibration site age 58 years into the past for those records, introducing small systematic errors (per mil range) into our ^{10}Be production rate and exposure age calculations. It is important to note that the magnitude of these errors depends on the age of the landform being dated, and that of the calibration site, as they may sample different portions of the underlying geomagnetic framework.

Using OxCal 4.0.5, we derived a mean age for the Macaulay valley debris-flow diamicton of 9690 ± 50 cal yr before AD2008 (median = 9680 cal yr before AD2008; see Fig. 10). This forms the basis for our ^{10}Be production-rate calibration and aligns well with calibrated values for radiocarbon dates reported by Grant-Taylor and Rafter (1971); 9420 ± 140 cal yr before AD2008) and McSaveney and Whitehouse (1989); 9750 ± 170 cal yr before AD2008).

4.1.2. ^{10}Be data

All ^{10}Be data are reported in Table 2. All uncertainties are reported at the 1σ level, unless otherwise noted. The seven measured ^{10}Be concentrations exhibit low analytical uncertainties (2–3%) and overlap at 1σ, forming an approximately normal distribution with a mean concentration of 87 100 ± 1600 at g^{-1}, and a reduced-χ^2 of 0.60 (Fig. 12). In this case, the maximum χ^2 expected to yield a single Gaussian distribution at 95% confidence, minus 1° of freedom, is 12.59. We obtained a χ^2 value of 3.61. Therefore, the χ^2 reported here, which is less than the expected value, indicates that all inter-sample variability could be explained by analytical uncertainty alone (Bevington and Robinson, 1992). Natural processes compromising the surface-exposure dating approach, such as snow or vegetation cover of the exposed surface, prior exposure of the boulders, or post-depositional rotation or exhumation of individual boulders, must be insignificant (Balco and Schaefer, 2006), as they would provide a different exposure history for each boulder.

The local production rate determined at the Macaulay site is 8.99 ± 0.17 at g yr^{-1}. In order to permit comparison of calibration experiments at different locations, reported production rates are referenced to sea level and high latitude in Table 3a. Following Balco et al. (2009), we determined best-fit reference ^{10}Be production rates applicable to the five production-rate scaling schemes implemented in Balco et al. (2008) by choosing the value of the reference production rate that minimized the least-squares misfit between the calculated and independently determined exposure age for the site. Reference ^{10}Be production rates, shown in bold in Table 3a, are normalized to 07KNSTD (Nishiizumi et al., 2007) and

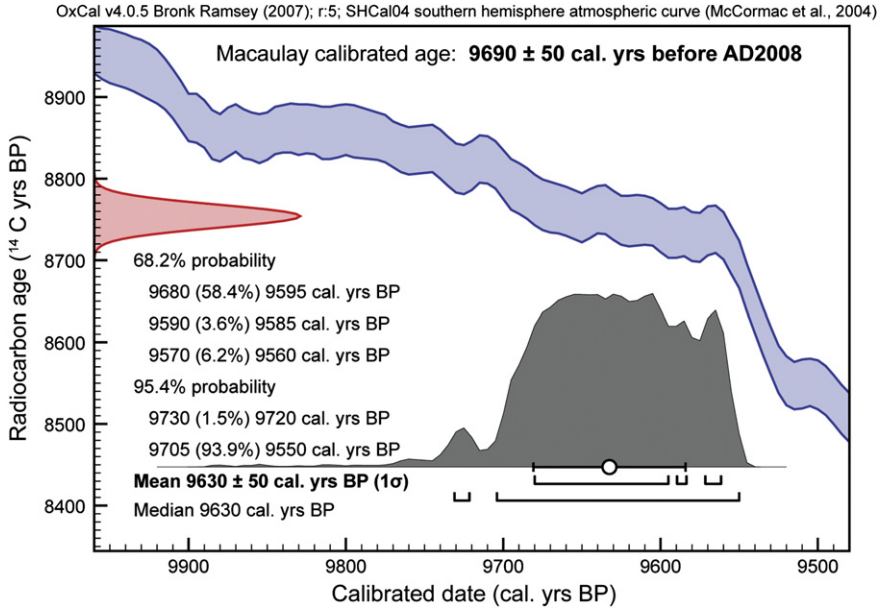

Fig. 11. Radiocarbon calibration output for the Macaulay valley samples. Vertical axis gives radiocarbon ages (in ^{14}C yrs BP), with buried soil age distribution plotted as red curve. Blue line is the SHCal04 calibration curve (McCormac et al., 2004). Horizontal axis shows calibration output, with units expressed in 'cal. yrs BP'. Grey area is calibrated probability distribution of the radiocarbon dates, accompanied by summary statistics. Ages printed in bold are in 'cal. yrs BP' and 'cal. yrs before AD2008', respectively, the latter of which is used in subsequent calibration calculations. (For interpretation of the references to colour in this figure legend, the reader is referred to the web version of this article.)

Please cite this article in press as: Putnam, A.E., et al., In situ cosmogenic ^{10}Be production-rate calibration from the Southern Alps, New Zealand, Quaternary Geochronology (2010), doi:10.1016/j.quageo.2009.12.001

Table 2
Exposure sample details and ^{10}Be data.

CAMS laboratory no.	Sample ID	Latitude (DD)	Longitude (DD)	Elevation (m a.s.l.)	Boulder size ($L \times W \times H$) (cm)	Sample thickness (cm)	Shielding correction	Quartz weight (g)	Carrier added (mg)[a]	^{10}Be/^{9}Be $\pm 1\sigma$ (10^{-14})[b]	[^{10}Be] $\pm 1\sigma$ (10^4 atoms g^{-1})	Average ^{9}Be current (μA)[c]
Macaulay valley debris-flow deposit												
BE25396	MR-08-01	−43.57605	170.60835	1024.9	302 × 262 × 119	0.82	0.992	12.1291	0.2000	7.97 ± 0.17	8.75 ± 0.19	17.9 (3)
BE25397	MR-08-02	−43.57581	170.60857	1024.5	320 × 150 × 96	1.04	0.993	15.5341	0.2014	10.62 ± 0.30	9.17 ± 0.26	22.3 (2)
BE25398	MR-08-03	−43.57452	170.60805	1029.4	250 × 180 × 138	1.85	0.988	11.9735	0.2015	7.84 ± 0.15	8.78 ± 0.17	22.1 (3)
BE25399	MR-08-04	−43.57444	170.60832	1028.4	205 × 190 × 121	0.83	0.989	15.0788	0.2013	9.97 ± 0.24	8.86 ± 0.22	24.0 (2)
BE25400	MR-08-05	−43.57435	170.60760	1032.1	280 × 240 × 140	1.57	0.991	14.8377	0.2013	9.93 ± 0.27	8.97 ± 0.24	22.2 (4)
BE25401	MR-08-13	−43.57751	170.60695	1027.6	180 × 150 × 68	1.69	0.991	13.6681	0.2011	9.15 ± 0.18	8.96 ± 0.18	20.1 (3)
BE25402	MR-08-14	−43.57787	170.60493	1032.0	390 × 330 × 125	2.16	0.991	15.0428	0.2020	9.85 ± 0.20	8.81 ± 0.17	23.7 (3)
BE25395	Blank2 18April08	–	–	–	–	–	–	–	0.2008	0.10 ± 0.02	–	22.0 (3)
Boundary Stream tarn moraines												
Outer ridge												
BE26113	BST-08-02	−44.02953	170.11850	872.6	140 × 100 × 50	2.17	0.995	6.7583	0.1993	7.84 ± 0.21	14.90 ± 0.41	16.5 (2)
BE26121	BST-08-10	−44.04680	170.12028	838.4	200 × 150 × 103	1.62	0.998	7.0753	0.2015	7.83 ± 0.27	14.84 ± 0.51	9.6 (2)
BE26122	BST-08-11	−44.03631	170.11805	857.0	200 × 100 × 50	2.38	0.993	7.0878	0.2015	7.72 ± 0.22	14.60 ± 0.42	13.5 (2)
Inner recessional ridges												
BE26114	BST-08-03	−44.03131	170.11922	852.0	160 × 80 × 73	2.22	0.995	6.7250	0.2007	7.36 ± 0.28	14.62 ± 0.47	14.7 (4)
BE26115	BST-08-04	−44.03426	170.12025	839.3	120 × 100 × 75	2.35	0.996	7.0238	0.2011	7.77 ± 0.21	14.81 ± 0.40	17.1 (2)
BE26116	BST-08-05	−44.03728	170.12081	837.1	200 × 130 × 80	2.16	0.997	7.0186	0.2013	7.56 ± 0.19	14.44 ± 0.36	16.9 (3)
BE26117	BST-08-06	−44.03773	170.11992	835.1	130 × 100 × 56	1.07	0.997	7.0161	0.2014	7.78 ± 0.28	14.87 ± 0.54	10.5 (4)
BE26118	BST-08-07	−44.03985	170.11979	831.9	180 × 120 × 80	2.00	0.997	7.0500	0.2009	7.71 ± 0.21	14.63 ± 0.40	15.5 (2)
BE26119	BST-08-08	−44.04216	170.12218	831.4	270 × 200 × 75	1.31	0.998	7.0302	0.2009	7.88 ± 0.17	15.00 ± 0.33	16.1 (3)
BE26120	BST-08-09	−44.04446	170.12274	823.3	190 × 190 × 98	1.80	0.998	7.0126	0.2017	7.56 ± 0.20	14.47 ± 0.39	16.4 (2)
BE26124	Blank 20Aug08	–	–	–	–	–	–	–	0.2017	0.07 ± 0.02	–	13.6 (2)

[a] Carrier ^{9}Be concentration is 996 ppm.
[b] Reported blank-corrected ratios and concentrations are referenced to 07KNSTD (2.85×10^{-12}; Nishiizumi et al., 2007).
[c] $^{9}Be^{+3}$ measured after the accelerator. Reported currents are averaged over all AMS runs for a given sample. The number of AMS runs is given in parentheses.

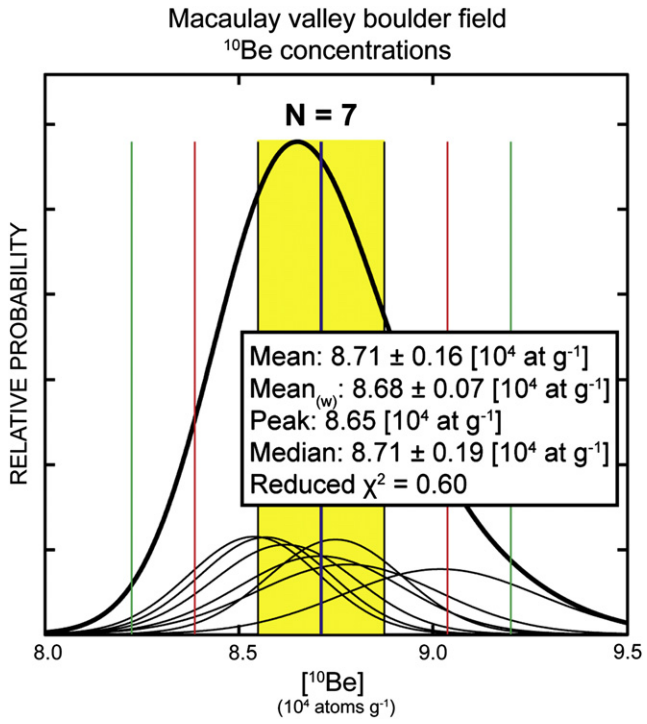

Fig. 12. Camel plot of the Macaulay valley boulder field boulder-surface ^{10}Be concentrations. Concentrations in this diagram have been corrected for shielding and thickness. Although no adjustments for elevation have been applied, the elevation difference between boulders is small (<10 m) and will likely have an insignificant impact on ^{10}Be concentrations as displayed. Gaussian probability curves for individual concentrations are given as gray lines, with summed probability plotted in black. Black, red, and green vertical lines mark one, two, and three standard deviations, respectively. The blue vertical line denotes the mean value. Summary statistics are in inset (For interpretation of the references to colour in this figure legend, the reader is referred to the web version of this article.).

incorporate the geomagnetic characterization of Lifton et al. (2008), which is resolved at 100-yr steps over the last 50 000 yrs. By this method, reference SLHL ^{10}Be production rates ('P_{NZ2}' in Table 3b), including only the local time-dependent production-rate errors are 3.84 ± 0.08 at g yr^{-1} (St), 3.87 ± 0.08 at g yr^{-1} (De), 3.83 ± 0.08 at g yr^{-1} (Du), 4.15 ± 0.09 at g yr^{-1} (Li), and 3.74 ± 0.08 at g yr^{-1} (Lm). Uncertainties for the local, time-integrated production rates are only ~2%, owing to the tight internal consistency of the ^{14}C and ^{10}Be datasets. There is a 1.07% scatter in ages calculated at SLHL due to discrepancies among scaling methods. A propagation of the local production-rate uncertainty with this SLHL scaling uncertainty yields 'external' uncertainties of 2.3% (St, De, and Du) and 2.4% (Li, Lm). We note, however, that scaling uncertainty varies in time and space, so we caution that this stated uncertainty might underestimate the true scaling uncertainty by an unknown amount in other regions (e.g., high-altitude tropical regions).

To expedite comparison with earlier results, production rates normalized to KNSTD and using the geomagnetic field characterization of Lifton et al. (2005), as modified by Balco et al. (2008), are also given in Table 3a. For reference, we include in Table 3b the SLHL production-rate estimates for each scaling method based on the 'global' calibration dataset (Balco et al., 2008) and northeastern North American data (Balco et al., 2009), here abbreviated as 'NENA'. The global calibration and NENA results have been normalized to 07KNSTD by applying a conversion factor of 0.904 (Nishiizumi et al., 2007). In addition to the 'reference' Macaulay values, we also provide the Macaulay production rates calculated using the same geomagnetic framework, attenuation length, and calendar-age reference as the global and NENA rates. We have also calculated and propagated an SLHL scaling uncertainty of 1.5% into the local time-integrated uncertainty for these alternate values.

The production rates presented here are significantly lower than those of the global calibration dataset, showing a ~11–13% offset for all scaling schemes when normalized to the same standard, reference to AD 1950, and calculated using the same geomagnetic model

Table 3a
Reference SLHL ^{10}Be production rates determined from the Macaulay valley debris-flow deposit, calculated with the scaling methods included in Balco et al. (2008), and with the geomagnetic framework of Balco et al. (2008) and Lifton et al. (2008), abbreviated as "Ba08" and "Li08", respectively. Production rates have been normalized to both the 07KNSTD and KNSTD AMS ^{10}Be standards, indicated in subscript. Recommended reference production rates given in bold text are calculated using the most recent standard (07KNSTD) and the high-resolution geomagnetic model of Lifton et al. (2008). Values bound by parentheses are 1σ uncertainties expressed as percentages.

Scaling Scheme ID	$P_{NZ/07KNSTD/Li08}$ (atoms g^{-1} a^{-1})	χ^2_r	$P_{NZ/07KNSTD/Ba08}$ (atoms g^{-1} a^{-1})	χ^2_r	$P_{NZ/KNSTD/Li08}$ (atoms g^{-1} a^{-1})	χ^2_r	$P_{NZ/KNSTD/Ba08}$ (atoms g^{-1} a^{-1})	χ^2_r
St	**3.84 ± 0.08 (2.1%)**	**0.38**	3.84 ± 0.08 (2.1%)	0.38	4.25 ± 0.09 (2.1%)	0.34	4.25 ± 0.09 (2.1%)	0.34
De	**3.87 ± 0.08 (2.1%)**	**0.41**	3.88 ± 0.08 (2.1%)	0.39	4.28 ± 0.09 (2.1%)	0.36	4.29 ± 0.09 (2.1%)	0.35
Du	**3.83 ± 0.08 (2.1%)**	**0.39**	3.87 ± 0.08 (2.1%)	0.39	4.23 ± 0.09 (2.1%)	0.34	4.28 ± 0.09 (2.1%)	0.35
Li	**4.15 ± 0.09 (2.2%)**	**0.42**	4.18 ± 0.09 (2.2%)	0.41	4.59 ± 0.10 (2.2%)	0.37	4.62 ± 0.10 (2.2%)	0.36
Lm	**3.74 ± 0.08 (2.1%)**	**0.40**	3.76 ± 0.08 (2.1%)	0.39	4.13 ± 0.09 (2.2%)	0.35	4.15 ± 0.09 (2.2%)	0.34

Table 3b
Comparison of production rates using scaling methods given in Balco et al. (2008). These production rates have been normalized to the 07KNSTD standard to maintain consistency when comparing to previously published estimates. 'GLOBAL' refers to the production rates determined from the global calibration dataset (Balco et al., 2008); 'NENA' refers to production rates presented in Balco et al. (2009); and 'NZ' refers to the New Zealand production rates presented in this study. P_{NZ1} is calculated using radiocarbon calibration relative to years before 1950 ('yrs BP'), incorporates an attenuation length of 160 g cm^{-2}, and uses the 'Ba08' geomagnetic framework; consistent with the methods of Balco et al. (2008, 2009). The P_{NZ1} values are directly comparable to the published P_{GLOBAL} and P_{NENA} rates. P_{NZ2} refers to the recommended production-rate calculation based on the radiocarbon age of the Macaulay valley debris flow in terms of calendar years before AD2008, uses an attenuation length of 177 g cm^{-2} (after Farber et al., 2008), and implements the 'Li08' geomagnetic model. Errors include scaling uncertainty at sea level and high latitude. Note that P_{NZ1} and P_{NZ2} production rates are indistinguishable within uncertainties, despite differences in how the values were calculated.

Scaling Scheme ID	P_{GLOBAL} (atoms g^{-1} a^{-1})	P_{NENA} (atoms g^{-1} a^{-1})	P_{NZ1} (atoms g^{-1} a^{-1})	Ratio P_{NZ1}/ P_{GLOBAL}	Ratio P_{NZ1}/ P_{NENA}	P_{NZ2} (atoms g^{-1} a^{-1})	Ratio P_{NZ2}/ P_{GLOBAL}	Ratio P_{NZ2}/ P_{NENA}
St	4.47 ± 0.40 (9%)	3.91 ± 0.19 (4.8%)	**3.88 ± 0.10 (2.5%)**	0.87	0.99	**3.84 ± 0.09 (2.3%)**	0.86	0.98
De	4.40 ± 0.53 (12%)	4.10 ± 0.20 (4.9%)	**3.91 ± 0.10 (2.5%)**	0.89	0.95	**3.87 ± 0.09 (2.3%)**	0.88	0.94
Du	4.42 ± 0.53 (12%)	4.13 ± 0.20 (4.9%)	**3.91 ± 0.10 (2.5%)**	0.88	0.95	**3.83 ± 0.09 (2.3%)**	0.87	0.94
Li	4.85 ± 0.49 (10%)	4.47 ± 0.22 (4.9%)	**4.22 ± 0.11 (2.6%)**	0.87	0.94	**4.15 ± 0.10 (2.4%)**	0.86	0.93
Lm	4.37 ± 0.39 (9%)	3.85 ± 0.19 (4.9%)	**3.79 ± 0.10 (2.6%)**	0.87	0.98	**3.74 ± 0.09 (2.4%)**	0.86	0.97

Please cite this article in press as: Putnam, A.E., et al., In situ cosmogenic ^{10}Be production-rate calibration from the Southern Alps, New Zealand, Quaternary Geochronology (2010), doi:10.1016/j.quageo.2009.12.001

Table 4
Radiocarbon data assayed from the BST sediments, reproduced from Vandergoes et al. (2008). Ages shown in italics were identified by Vandergoes et al. (2008) as outliers with respect to the age model developed for the data set.

Core	Sub-bottom depth (cm) core 0201	Sub-bottom depth (cm) from 0408 relative to 0201	^{14}C lab no.	δ^{13}C (‰)	^{14}C age $\pm 1\sigma$ (^{14}C yrs BP)	(BP)	Calibrated age (cal yrs) (Before, 2008)	1σ
201	308		Wk-10719	−29.9	9990 ± 75	11 500	11 650	160
201	316		OS-37971	−24.42	10 100 ± 40	11 700	11 760	130
201	317		OS-42553	−28.15	*9870 ± 65*	*11 310*	*11 370*	*100*
201	333		OS-42661	−20.73	10 200 ± 45	11 910	11 965	95
201	334		OS-37972	−21.09	10 400 ± 50	12 300	12 360	140
408		360	OS-48412	−22.36	10 350 ± 55	12 220	12 280	130
408		380	OS-46017	−21.9	11 100 ± 70	13 015	13 075	65
408		380	OS-45812	−22.11	11 150 ± 45	13 050	13 110	55
201	382		OS-38191	−21.43	11 050 ± 65	12 980	13 040	60
201	394		OS-42662	−21.86	*10 800 ± 60*	*12 825*	*12 853*	*35*
201	410		OS-38192	−22.72	12 150 ± 70	14 005	14 065	90
408		410	OS-45813	−22.99	12 300 ± 45	14 210	14 270	140
408		410	OS-46018	−23.07	12 300 ± 45	14 210	14 270	140
408		450	OS-48413	−21.63	12 600 ± 55	14 830	14 890	160
201	483		OS-42663	−20.13	13 200 ± 60	15 640	15 700	180
201	528		OS-38193	−19.71	14 100 ± 65	16 800	16 860	200
201	532		OS-42664	−18.93	14 800 ± 65	18 000	18 060	210

(Table 4). All uncertainties outlined above are well within the 11–13% difference. Macaulay production-rate values referenced to AD2008 and calculated using the updated high-resolution geomagnetic framework are 12–14% lower than those of the global calibration dataset. The New Zealand values are slightly below the lower error bounds of those obtained using the global calibration dataset (9–12%; Balco et al., 2008). Our results are in better agreement, however, with the NENA production rates determined by Balco et al. (2009), based on surface ^{10}Be concentrations of boulders embedded in lateglacial moraines that are chronologically bracketed by radiocarbon-dated sections of the Connecticut Valley varve sequence (e.g., Antevs, 1922, 1928; Ridge et al., 1999; Thompson et al., 1999), as well as ^{10}Be concentrations from boulders embedded in a radiocarbon-dated ice-contact glaciomarine delta in northeastern Baffin Island (Briner et al., 2007; Balco et al., 2009). We note that calibrating the New Zealand production rate to radiocarbon ages referenced to 'years before AD2008' is responsible for about 0.6% of the observed offset between the production rates presented here and those of Balco et al. (2008, 2009), who referenced production rates to years BP (i.e., years before AD1950; Table 3b).

4.2. A last glacial maximum test case for the Holocene production-rate values: the boundary stream tarn moraines

4.2.1. Radiocarbon data

Vandergoes et al. (2008) obtained seventeen radiocarbon dates from two composite cores in the BST pond (Table 4). They employed

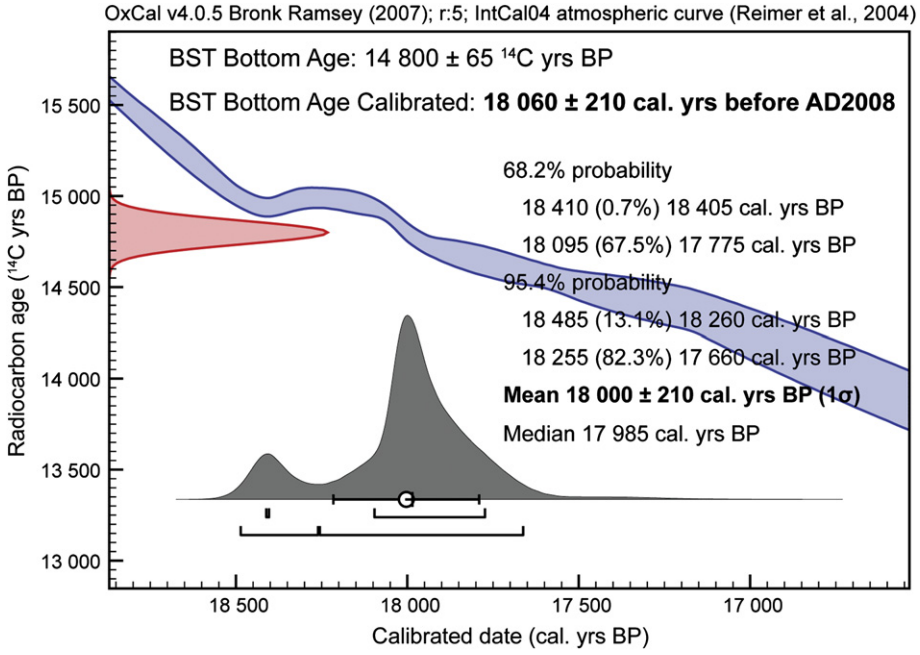

Fig. 13. Radiocarbon calibration output for the BST basal radiocarbon age (sample OS-42664) represented by the red area. Vertical axis gives radiocarbon age (in ^{14}C yrs BP) and the blue area is the IntCal04 calibration curve (Reimer et al., 2004). Horizontal axis shows calibration output, with units expressed in 'cal. yrs BP'. Grey area depicts the calibrated probability distribution, accompanied by summary statistics. Ages printed in bold are in 'cal. yrs BP' and 'cal. yrs before AD2008'. (For interpretation of the references to colour in this figure legend, the reader is referred to the web version of this article.)

Table 5
^{10}Be ages of boulder samples from the Boundary Stream tarn moraines, calculated using scaling factors and geomagnetic models presented in Balco et al. (2008), and production rates of Balco et al. (2008, 2009), and this study, described as P_{GLOBAL}, P_{NENA}, and P_{NZ2}, respectively. Ages are given in thousands of years (kyrs) before AD2008.

Sample ID	P_{GLOBAL}					P_{NENA}					P_{NZ2}				
	St Age (kyrs)	De Age (kyrs)	Du Age (kyrs)	Li Age (kyrs)	Lm Age (kyrs)	St Age (kyrs)	De Age (kyrs)	Du Age (kyrs)	Li Age (kyrs)	Lm Age (kyrs)	St Age (kyrs)	De Age (kyrs)	Du Age (kyrs)	Li Age (kyrs)	Lm Age (kyrs)
Outer ridge															
BST-08-02	15.74 ± 0.44	16.31 ± 0.45	16.24 ± 0.45	16.01 ± 0.44	15.74 ± 0.44	18.00 ± 0.50	17.47 ± 0.48	17.37 ± 0.48	17.36 ± 0.48	17.84 ± 0.49	18.31 ± 0.51	18.41 ± 0.51	18.47 ± 0.51	18.49 ± 0.51	18.23 ± 0.50
BST-08-10	16.01 ± 0.55	16.60 ± 0.57	16.54 ± 0.57	16.30 ± 0.56	16.01 ± 0.55	18.31 ± 0.63	17.79 ± 0.61	17.69 ± 0.61	17.67 ± 0.61	18.15 ± 0.62	18.63 ± 0.64	18.75 ± 0.64	18.81 ± 0.65	18.84 ± 0.65	18.54 ± 0.64
BST-08-11	15.70 ± 0.46	16.27 ± 0.48	16.20 ± 0.47	15.98 ± 0.47	15.70 ± 0.46	17.95 ± 0.52	17.43 ± 0.51	17.33 ± 0.51	17.32 ± 0.51	17.79 ± 0.52	18.25 ± 0.53	18.36 ± 0.54	18.42 ± 0.54	18.45 ± 0.54	18.17 ± 0.53
Inner recessional crests															
BST-08-03	15.73 ± 0.51	16.31 ± 0.53	16.24 ± 0.53	16.02 ± 0.52	15.73 ± 0.51	17.99 ± 0.58	17.47 ± 0.57	17.37 ± 0.56	17.36 ± 0.56	17.83 ± 0.58	18.29 ± 0.59	18.41 ± 0.60	18.47 ± 0.60	18.50 ± 0.51	18.21 ± 0.59
BST-08-04	16.10 ± 0.43	16.69 ± 0.45	16.63 ± 0.45	16.39 ± 0.44	16.10 ± 0.43	18.41 ± 0.50	17.88 ± 0.48	17.78 ± 0.48	17.77 ± 0.48	18.24 ± 0.49	18.72 ± 0.50	18.84 ± 0.51	18.90 ± 0.51	18.93 ± 0.51	18.63 ± 0.50
BST-08-05	15.68 ± 0.39	16.27 ± 0.41	16.20 ± 0.40	15.98 ± 0.40	15.69 ± 0.39	17.93 ± 0.45	17.43 ± 0.43	17.33 ± 0.43	17.32 ± 0.43	17.78 ± 0.44	18.24 ± 0.45	18.36 ± 0.46	18.42 ± 0.46	18.45 ± 0.46	18.16 ± 0.45
BST-08-06	16.03 ± 0.59	16.63 ± 0.61	16.56 ± 0.61	16.32 ± 0.60	16.03 ± 0.59	18.33 ± 0.67	17.81 ± 0.65	17.71 ± 0.65	17.70 ± 0.65	18.17 ± 0.67	18.54 ± 0.68	18.78 ± 0.69	18.85 ± 0.69	18.87 ± 0.69	18.57 ± 0.68
BST-08-07	15.94 ± 0.44	16.54 ± 0.45	16.47 ± 0.45	16.24 ± 0.45	15.94 ± 0.44	18.22 ± 0.50	17.71 ± 0.49	17.61 ± 0.48	17.60 ± 0.48	18.07 ± 0.50	18.54 ± 0.51	18.67 ± 0.51	18.73 ± 0.51	18.76 ± 0.51	18.46 ± 0.51
BST-08-08	16.23 ± 0.35	16.84 ± 0.37	16.77 ± 0.37	16.53 ± 0.36	16.23 ± 0.35	18.56 ± 0.41	18.04 ± 0.39	17.94 ± 0.39	17.92 ± 0.39	18.40 ± 0.40	18.89 ± 0.41	19.02 ± 0.42	19.08 ± 0.42	19.11 ± 0.42	18.80 ± 0.41
BST-08-09	15.82 ± 0.43	16.42 ± 0.44	16.35 ± 0.44	16.13 ± 0.44	15.83 ± 0.43	18.09 ± 0.49	17.59 ± 0.47	17.49 ± 0.47	17.48 ± 0.47	17.94 ± 0.48	18.40 ± 0.50	18.54 ± 0.50	18.60 ± 0.50	18.63 ± 0.50	18.33 ± 0.49
Mean ± 1σ	**15.90 ± 0.19**	**16.49 ± 0.20**	**16.42 ± 0.20**	**16.19 ± 0.20**	**15.90 ± 0.19**	**18.18 ± 0.22**	**17.66 ± 0.21**	**17.56 ± 0.22**	**17.55 ± 0.21**	**18.02 ± 0.20**	**18.49 ± 0.23**	**18.61 ± 0.23**	**18.67 0.23**	**18.70 ± 0.23**	**18.41 ± 0.22**

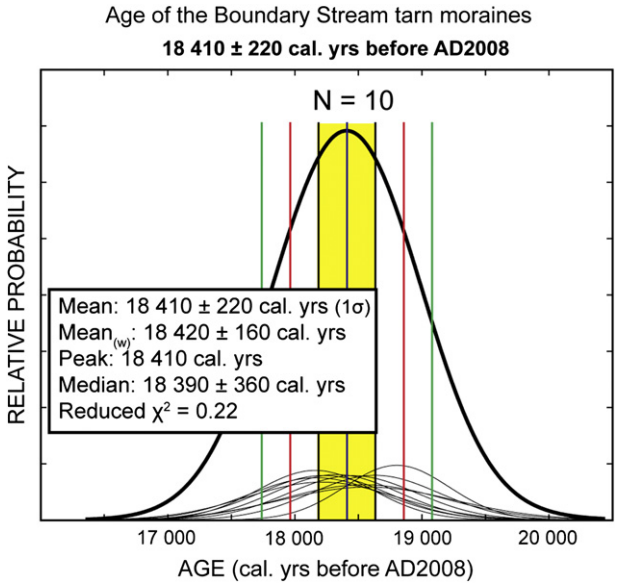

Fig. 14. Camel plot of the BST moraine complex ^{10}Be surface-exposure ages. Ages are calculated using the 'P_{NZ2}' production rate determined from the Macaulay valley calibration site, and the 'Lm' scaling method. Using the P_{NZ1} rate and/or other scaling models would shift the distribution systematically to slightly different values, but the internal consistency of the dataset would not change. Gaussian probability curves for individual ages are given as gray lines while the black line represents the summed probability, accompanied by summary statistics. Black, red, and green vertical lines mark one, two, and three standard deviations, respectively, while the blue vertical line denotes the mean value (For interpretation of the references to colour in this figure legend, the reader is referred to the web version of this article.).

the technique of Blaauw and Christen (2005) to construct an age model for the cores, and this procedure identified two dates as outliers (OS 42553, OS 42662). The remaining dates show a high degree of internal consistency. The lowest sample was assayed from organic matter within the upper 10 cm of the basal diamicton, and returned an age of 14 800 ± 65 ^{14}C yrs BP. The calibrated calendar age is 18 060 ± 210 cal yr before AD2008, based on the IntCal04 curve (Reimer et al., 2004) and calculated with the OxCal 4.0.5 program (Fig. 13). This basal date thus affords a minimum estimate of when the BST site became ice-free and lacustrine sediment began to accumulate in the pond, and therefore represents a minimum limit for when the adjacent moraines were formed.

4.2.2. ^{10}Be data

^{10}Be concentrations of ten boulder samples from the BST moraines are given in Table 2. Corresponding exposure ages are given in Table 5, calculated with the global calibration dataset (Balco et al., 2008), the NENA dataset (Balco et al., 2009), and the New Zealand values presented here (NZ). Average site-specific production rates, scaled from the Macaulay site values, are 7.84 at $g^{-1}\,yr^{-1}$ (St), 7.90 at $g^{-1}\,yr^{-1}$ (De), 7.91 at $g^{-1}\,yr^{-1}$ (Du), 7.92 at $g^{-1}\,yr^{-1}$ (Li), and 7.82 at $g^{-1}\,yr^{-1}$ (Lm), and scaling factors are 0.87 (St, Lm) and 0.88 (De, Du, Li). ^{10}Be ages agree internally to within 1.2%, showing a high level of consistency (Fig. 14). The distribution yields a χ^2 of 1.99, a value that is significantly less than the expected maximum χ^2 of 16.92. This result indicates that analytical uncertainty alone can explain all of the sample variability.

The mean landform-age calculated for the BST moraines using ^{10}Be varies depending on the production rates used (Table 5). Using the five scaling methods, mean ages calculated using the recommended NZ production rate (P_{NZ2}) vary between about 18 410 and 18 700 cal yr before AD2008. Means calculated with the global production rate range from 15 900 to 16 490 cal yr before AD2008,

and those calculated using NENA range from 17 550 to 18 180 cal yr before AD2008. Overall, ^{10}Be ages show the closest consistency with the radiocarbon age from the basal sediments of BST when calculated using the NZ or NENA production rates. ^{10}Be ages are consistently younger than the minimum-limiting radiocarbon age when calculated with the global production rate.

5. Discussion

5.1. Implications for local exposure-age calculations

Applying the NZ (i.e., Macaulay valley) Holocene production rates for each scaling scheme, respectively, to ^{10}Be concentrations of boulder surfaces associated with the LGM BST moraines yields exposure ages that are consistent with the minimum-limiting radiocarbon age constraints. This result indicates that the NZ production rate determined at Macaulay valley is applicable to local sites exposed at least since ~19 000 yr ago. At face value, this apparent consistency between interglacial and glacial production-rate values implies that any SLP changes in New Zealand since the end of the last ice age were sufficiently small to be of little consequence for the long-term production rate. This finding is consistent with the modeling results of Staiger et al. (2007).

Given the successful performance of the Macaulay production rates at the BST test site, we suggest that the local reference production rates presented here be used to calculate exposure ages in New Zealand. When calculating ages in New Zealand located at similar altitudes to the Macaulay calibration site, we suggest propagating the local systematic production-rate uncertainty of 2.2% with reported landform ^{10}Be exposure-age uncertainties. When using the Macaulay production rates outside of New Zealand, we suggest propagating the 'external' uncertainties that include an SLHL scaling error (~2.4%). If comparing exposure ages based on the New Zealand production rate with radiocarbon data, either the calibrated radiocarbon ages should be corrected for the number of years elapsed between AD1950 and when the surface-exposure samples were collected, the surface-exposure ages should be corrected to correspond to the number of years before AD1950, or all ages should be presented as years AD/BC (alternatively 'CE/BCE'). As mentioned above, it is worth considering that a small uncertainty arises from a 58-yr offset between the AD1950 'time zero' of the palaeomagnetic and solar records used in the time-dependent scaling models, and the AD2008 'time zero' adopted in this study.

5.2. Comparison of different ^{10}Be production-rate determinations

As shown in Section 4.2.2, exposure ages calculated for the BST moraines agree best with radiocarbon constraints when calculated using the production rates determined from the Macaulay valley (Fig. 15); the median ages derived by all scaling methods are older than the minimum age for these boulders defined by BST sediments. There is also broad similarity between exposure ages and the BST radiocarbon control when using the production-rate values of Balco et al. (2009) determined from NENA sites, although there is a noticeably larger deviation among scaling methods. Uncertainties involved in the large extrapolation of scaling parameters from the NENA calibration sites to New Zealand, as well as local effects such as uplift, may account for some component of the differences observed between ages calculated using the NENA and New Zealand production rates. When applying the global calibration dataset of Balco et al. (2008), all scaling methods give ^{10}Be ages that are systematically younger (by over three standard deviations) than the minimum-limiting radiocarbon age of deglaciation, and thus are not tenable. From this comparison, we speculate that the good agreement between the New Zealand and the NENA ^{10}Be production rates, both

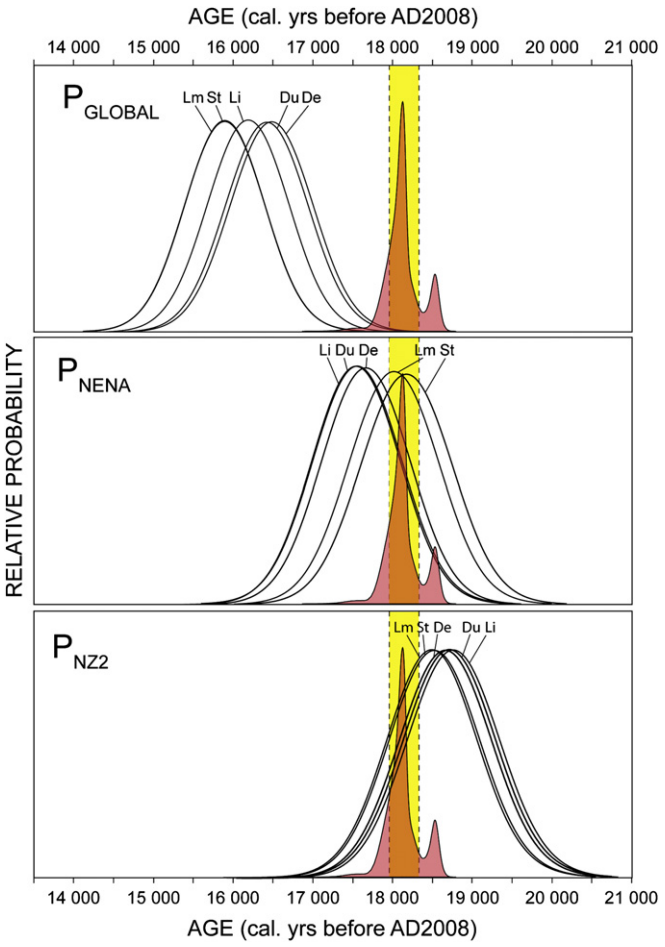

Fig. 15. Plot showing the ^{10}Be age distribution for the BST moraines, calculated using different production-rate calibrations and scaling schemes, for direct comparison with the local calibrated radiocarbon age obtained by Vandergoes et al. (2008), shown as filled red curve, adjusted to years before AD2008. Bold lines are summed probability distributions for the BST ^{10}Be data, calculated for different production rate and scaling combinations. Top panel shows the BST ^{10}Be age distribution calculated using the global calibration dataset of Balco et al. (2008); 'P_{GLOBAL}', middle panel shows the ^{10}Be age distribution calculated with the northeast North American production rates of Balco et al. (2009); 'P_{NENA}', and bottom panel displays the BST ^{10}Be age distribution calculated with the local Macaulay valley 'recommended' production rate (this study; 'P_{NZ2}'). We note that the recommended (P_{NZ2}) production rate, which incorporates the high-resolution Lifton et al. (2008) geomagnetic model and radiocarbon normalization to AD2008, is only ≤1% different from the P_{NZ1} rate, which uses a geomagnetic framework and calendar-age reference point (AD1950) comparable to P_{GLOBAL} and P_{NENA}. Thus using the P_{NZ2} rate yields ages that are virtually indistinguishable from those calculated with P_{NZ1}. All scaling methods are included in each panel, as indicated by solid lines and abbreviations defined in Section 3.4. Yellow boxes show the 1σ uncertainty range of the BST basal radiocarbon age. Horizontal axis is in years before AD2008. (For interpretation of the references to colour in this figure legend, the reader is referred to the web version of this article.)

of which are based on calibration sites with direct radiocarbon-based age control at the sites, indicates production-rate consistency where scaling models predict similar geomagnetic and atmospheric effects (cf. Lifton et al., 2008). On the other hand, our results imply that production rates based on the global calibration dataset of Balco et al. (2008) significantly underestimate exposure ages in New Zealand, similar to the cases presented by Balco and Schaefer (2006) and Balco et al. (2009). Reasons for the discrepancy between the NZ and global production rates are unclear. Balco et al. (2009) speculated on why results from NENA were significantly lower than the global rate, but were unable arrive at a robust conclusion. We defer to the careful examination of the problem by Balco et al. (2009), and maintain that,

Please cite this article in press as: Putnam, A.E., et al., In situ cosmogenic ^{10}Be production-rate calibration from the Southern Alps, New Zealand, Quaternary Geochronology (2010), doi:10.1016/j.quageo.2009.12.001

at the moment, we also are unable to provide reasons for this discrepancy that go beyond untested speculation. Therefore, we conclude that the production rates presented in our study should be suitable for calculating exposure ages from New Zealand sites, using internationally established scaling factors for altitude, and that the applicability of the Macaulay production rates beyond New Zealand remains uncertain.

6. Conclusion

The exceptional internal consistency of the ^{10}Be and ^{14}C values determined from a debris-flow deposit in the Macaulay valley, and the success of a local test of the resulting production rates for late LGM time, affords the first direct estimate of ^{10}Be production in New Zealand and in the Southern Hemisphere middle latitudes. These production rates can be used to calculate ages of New Zealand surfaces exposed during or since the last glacial period, using appropriate scaling methods. We recommend that a production-rate uncertainty of ~2.2% be incorporated as a systematic error into surface-exposure age datasets developed at sites with similar altitudes to the Macaulay site in New Zealand using these production-rate values. When calculating surface-exposure ages outside of New Zealand with the NZ production rates, we suggest propagating an uncertainty of 2.3–2.4%, which includes an SLHL scaling uncertainty, with the overall landform-age uncertainty.

Acknowledgements

This work was supported by funding from the Gary C. Comer Science and Education Foundation (CSEF), the National Oceanographic and Atmospheric Administration (NOAA), and by National Science Foundation grants EAR-0745781, EAR-0345150 (CRONUS-Earth Project), and OCE-0753487 (NOSAMS). We thank the Department of Conservation – Te Papa Atawhai, Te Rünanga o Ngäi Tahu, and M. and G. Seymour of Ferintosh Station for granting us permission to access and collect samples from the field sites. We are grateful to the Mackenzie Alpine Trust and T. and K. Ritchie of Lake Ruataniwha Holiday Park for accommodation. S.L. Callard and M. Ryan assisted with fieldwork. B.G. Andersen provided invaluable wisdom and guidance. The staff of the LLNL Center for Accelerator Mass Spectrometry provided invaluable assistance during the ^{10}Be measurements reported here. We thank M.J. McSaveney and T.R.H. Davies for valuable discussions regarding possible New Zealand calibration sites. S.C. Cox, P. Upton, and P.O. Koons offered valuable expertise concerning the glacioisostatic and tectonic dynamics of the Southern Alps. G. Balco, N. Lifton, and one anonymous reviewer provided thoughtful and constructive reviews. A.E. Putnam was supported by fellowships from the CSEF and NOAA, as well as an assistantship from the University of Maine Department of Earth Sciences while conducting this research. M. Vandergoes and D.J.A. Barrell were supported by Foundation for Research, Science and Technology contract CO5X0701. This is LDEO contribution # 7315.

Editorial Handling by: D. Bourles.

References

Ackert Jr., R.P., Singer, B.S., Guillou, H., Kaplan, M.R., Kurz, M.D., 2003. Long-term cosmogenic ^{3}He production rates from ^{40}Ar/^{39}Ar and K–Ar dated Patagonian lava flows at 47°S. Earth and Planetary Science Letters 210, 119–136.

Ackert Jr., R.P., Becker, R.A., Singer, B.S., Kurz, M.D., Caffee, M.W., Mickelson, D.M., 2008. Patagonian glacier response during the late glacial–Holocene transition. Science 321, 392–395.

Amos, C.B., Burbank, D.W., Nobes, D.C., Read, S.A.L., 2007. Geomorphic constraints on listric thrust faulting: implications for active deformation in the Mackenzie basin, south Island, New Zealand. Journal of Geophysical Research 112, B03S11.

Antevs, E., 1922. The Recession of the Last Ice Sheet in New England: Research Series No. 11. American Geographical Society.

Antevs, E., 1928. The Last Glaciation with Special Reference to the Ice Sheet in North America: Research Series No. 17. American Geographical Society.

Balco, G., Schaefer, J.M., 2006. Cosmogenic-nuclide and varve chronologies for the deglaciation of southern New England. Quaternary Geochronology 1, 15–28.

Balco, G., Stone, J.O., Lifton, N.A., Dunai, T.J., 2008. A complete and easily accessible means of calculating surface exposure ages or erosion rates from ^{10}Be and ^{26}Al measurements. Quaternary Geochronology 3, 174–195.

Balco, G., Briner, J., Finkel, R.C., Rayburn, J.A., Ridge, J.C., Schaefer, J.M., 2009. Regional beryllium-10 production rate calibration for late-glacial northeastern North America. Quaternary Geochronology 4, 93–107.

Barrows, T.T., Lehman, S.J., Fifield, L.K., De Deckker, P.D., 2007. Absence of cooling in New Zealand and the adjacent ocean during the Younger Dryas chronozone. Science 318, 86–89.

Batt, G.E., Kohn, B.P., Braun, J., McDougall, I., Ireland, T.R., 1999. New insight into the dynamic development of the Southern Alps, New Zealand, from detailed thermochronological investigation of the Matakeke Range pegmatites. In: Ring, U., Brandon, M., Lister, G., Willett, S. (Eds.), Special Volume on Exhumation Processes: Normal Faulting, Ductile Flow, and Erosion. Geological Society (London) Special Publication 154, pp. 261–282.

Batt, G.E., Braun, J., Kohn, B.P., McDougall, I., 2000. Thermochronological analysis of the dynamics of the southern Alps, New Zealand. Geological Society of America Bulletin 112, 250–266.

Beavan, J., Matheson, D., Denys, P., Denham, M., Herring, T., Hager, B., Molnar, P., 2004. A vertical deformation profile across the Southern Alps, New Zealand, from 3.5 years of continuous GPS data. In: van Dam, T., Francis, O. (Eds.), Proceedings of the Workshop: The State of GPS Vertical Positioning Precision: Separation of Earth Processes by Space Geodesy. Cahiers de Centre Européen de Géodynamique et Séismologie, vol. 23. Centre Européen de Géodynamique et Séismologie, Luxembourg, pp. 111–123.

Beavan, J., Ellis, S., Wallace, L., 2007. Kinematic constraints from GPS on oblique convergence of the Pacific and Australian plates, central south Island, New Zealand. In: Okaya, D., Stern, T., Davey, F. (Eds.), A Continental Plate Boundary: Tectonics at South Island, New Zealand. AGU Geophysical Monograph Series 125, pp. 75–94.

Beck, A.C., 1972. Post-Otiran moraines in canterbury: further comment. New Zealand Journal of Geology and Geophysics 15, 299.

Benn, D.I., Evans, D.J.A., 1998. Glaciers and Glaciation. Arnold, London.

Bevington, P., Robinson, D., 1992. Data Reduction and Error Analysis for the Physical Sciences. WCB McGraw-Hill.

Birkeland, P.W., 1982. Subdivision of Holocene glacial deposits, Ben Ohau Range, New Zealand, using relative-dating methods. Geological Society of America Bulletin 93, 433–449.

Blaauw, M., Christen, J.A., 2005. Radiocarbon peat chronologies and environmental change. Applied Statistics 54, 805–816.

Boezio, M., Carlson, P., Francke, T., Weber, N., Suffert, M., Hof, M., Menn, W., Simon, M., Stephens, S., Bellotti, R., Cafagna, F., Circella, M., DeMarzo, C., Finetti, N., Papini, P., Piccardi, S., Spillantini, P., Ricci, M., Casolino, M., DePascale, M., Morselli, A., Picozza, P., Sparvoli, R., Barbiellini, G., Schiavon, P., Vacchi, A., Zampa, N., Grimani, C., Mitchell, J., Ormes, J., Streitmatter, R., Bravar, U., Golden, R., Stochaj, S., 2000. Measurement of the flux of atmospheric muons with the CAPRICE94 apparatus. Physical Review D 62 (032007).

Briner, J., Overeem, I., Miller, G., Finkel, R., 2007. The deglaciation of clyde inlet, northeastern Baffin Island, Arctic Canada. Journal of Quaternary Science 22, 223–232.

Bronk Ramsey, C., van der Plicht, J., Weninger, B., 2001. 'Wiggle matching' radiocarbon dates. Radiocarbon 43, 381–389.

Bronk Ramsey, C., 2007. Oxcal 4.0 Manual. Oxcal Program 4.0.7. http://c14.arch.ox.ac.uk/oxcalhelp/hlp_contents.html.

Bunting, D.G., 1977. Lake Pukaki Shore-Line Stability: A Preliminary Engineering Geological Investigation. Unpublished M.Sc. thesis, University of Canterbury, New Zealand.

Burrows, C.J., 1972. Post-Otiran moraines in canterbury. New Zealand Journal of Geology and Geophysics 15, 296–299. Comment.

Cox, S.C., Barrell, D.J.A., 2007. Geology of the Aoraki Area. Institute of Geological and Nuclear Sciences 1:250,000 Geological Map 15. GNS Science, Lower Hutt, New Zealand, 1 sheet and 71 pp.

Desilets, D., Zreda, M., 2003. Spatial and temporal distribution of secondary cosmic-ray nucleon intensities and applications to in-situ cosmogenic dating. Earth and Planetary Science Letters 206, 21–42.

Desilets, D., Zreda, M., Prabu, T., 2006. Extended scaling factors for in situ cosmogenic nuclides: new measurements at low latitude. Earth and Planetary Science Letters 246, 265–276.

Dunai, T., 2001. Influence of secular variation of the magnetic field on production rates of in situ produced cosmogenic nuclides. Earth and Planetary Science Letters 193, 197–212.

Farber, D.L., Mériaux, A.-S., Finkel, R.C., 2008. Attenuation length for fast nucleon production of ^{10}Be derived from near-surface production profiles. Earth and Planetary Science Letters 274, 295–300.

Gosse, J.C., Phillips, F.M., 2001. Terrestrial in situ cosmogenic nuclides: theory and application. Quaternary Science Reviews 20, 1475–1560.

Grant-Taylor, T.L., Rafter, T.A., 1971. New Zealand radiocarbon age measurements – 6. New Zealand Journal of Geology and Geophysics 14, 364–402.

Grubbs, F.E., 1969. Procedures for detecting outlying observations in samples. Technometrics 11, 1–21.

Heisinger, B., Lal, D., Jull, A.J.T., Kubik, P., Ivy-Ochs, S., Knie, K., Nolte, E., 2002a. Production of selected cosmogenic radionuclides by muons: 2. Capture of negative muons. Earth and Planetary Science Letters 200, 357–369.

Heisinger, B., Lal, D., Jull, A.J.T., Kubik, P., Ivy-Ochs, S., Neumaier, S., Knie, K., Lazarev, V., Nolte, E., 2002b. Production of selected cosmogenic radionuclides by muons 1. Fast muons. Earth and Planetary Science Letters 200, 345–355.

Herman, F., Cox, S.C., Kamp, P.J.J., 2009. Low-temperature thermochronology and thermo-kinematic modeling of deformation, exhumation and development of topography in the central Southern Alps, New Zealand. Tectonics 28, TC5011.

Jackson, J., Ritz, J.-F., Siame, L., Raisbeck, G., Yiou, F., Norris, R., Youngson, J., Bennett, E., 2002. Fault growth and landscape development rates in Otago, New Zealand, using in situ cosmogenic ^{10}Be. Earth and Planetary Science Letters 195, 185–193.

Kamp, P.J.J., Green, P.F., White, S.H., 1989. Fission track analysis reveals character of collisional tectonics in New Zealand. Tectonics 8, 169–195.

Kaplan, M.R., Moreno, P.I., Rojas, M., 2008. Glacial dynamics in southernmost South America during Marine Isotope Stage 5e to the Younger Dryas chron: a brief review with a focus on cosmogenic nuclide measurements. Journal of Quaternary Science 23, 649–658.

Kelly, M.A., 2003. The Late Würmian Age in the Western Swiss Alps – Last Glacial Maximum (LGM) ice-Surface Reconstruction and ^{10}Be Dating of Late-Glacial Features. Ph.D. dissertation, University of Bern, 105 pp.

Lal, D., 1991. Cosmic-ray labeling of erosion surfaces: in situ nuclide production rates and erosion models. Earth and Planetary Science Letters 104, 424–439.

Lal, D., Peters, B., 1967. Cosmic ray produced radioactivity on the earth. In: Sitte, K. (Ed.), Handbuch der Physik. Springer, Berlin, pp. 551–612.

Licciardi, J.M., 2000. Alpine Glacier and Pluvial Lake Records of Late Pleistocene Climate Variability in the Western United States. Ph.D. dissertation, Oregon State University, 155 pp.

Licciardi, J.M., Kurz, M.D., Curtice, J.M., 2006. Cosmogenic ^{3}He production rates from Holocene lava flows in Iceland. Earth and Planetary Science Letters 246, 251–264.

Lifton, N., Bieber, J., Clem, J., Duldig, M., Evenson, P., Humble, J., Pyle, R., 2005. Addressing solar modulation and long-term uncertainties in scaling secondary cosmic rays for in situ cosmogenic nuclide applications. Earth and Planetary Science Letters 239, 140–161.

Lifton, N., Smart, D., Shea, M., 2008. Scaling time-integrated in situ cosmogenic nuclide production rates using a continuous geomagnetic model. Earth and Planetary Science Letters 268, 190–201.

Little, T.A., Cox, S., Vry, J.K., Batt, G., 2005. Variations in exhumation level and uplift rate along the oblique-slip Alpine fault, central Southern Alps, New Zealand. Geological Society of America Bulletin 117, 707–723.

Mathews, W.H., 1967. Profiles of late Pleistocene glaciers in New Zealand. New Zealand Journal of Geology and Geophysics 10, 146–163.

McCormac, F.G., Hogg, A.G., Blackwell, P.G., Buch, C.E., Higham, T.F.G., Reimer, P.J., 2004. SHCal04 Southern hemisphere calibration, 0–11.0 cal kyr BP. Radiocarbon 46, 1087–1092.

McSaveney, M.J., Whitehouse, I.E., 1989. An early Holocene glacial advance in the Macaulay river valley, central Southern Alps, New Zealand. New Zealand Journal of Geology and Geophysics 32, 235–241.

Moar, N.T., 1980. Late Otiran and early Aranuian grassland in central south Island. New Zealand Journal of Ecology 3, 4–12.

Nishiizumi, K., Imamura, M., Caffee, M.W., Southon, J.R., Finkel, R.C., McAninch, J., 2007. Absolute calibration of ^{10}Be AMS standards. Nuclear Instruments and Methods in Physics Research B 258, 403–413.

Nishiizumi, K., Winterer, E., Kohl, C., Klein, J., Middleton, R., Lal, D., Arnold, J., 1989. Cosmic ray production rates of ^{26}Al and ^{10}Be in quartz from glacially polished rocks. Journal of Geophysical Research 94, 17907–17915.

Norris, R.J., Cooper, A.F., 2001. Late Quaternary slip rates and slip partitioning on the Alpine fault, New Zealand. Journal of Structural Geology 23, 507–520.

Pigati, J.S., Lifton, N.A., 2004. Geomagnetic effects on time-integrated cosmogenic nuclide production with emphasis on in situ ^{14}C and ^{10}Be. Earth and Planetary Science Letters 226, 193–205.

Reimer, P.J., et al., 2004. IntCal04 terrestrial radiocarbon age calibration, 0–26 cal kyr BP. Radiocarbon 46, 1029–1058.

Ridge, J., Besonen, M., Brochu, M., Brown, M., Callahan, S., Cook, J., Nicholson, R., Toll, N., 1999. Varve, paleomagnetic, and ^{14}C chronologies for late Pleistocene events in New Hampshire and Vermont (U.S.A.). Géographie Physique et Quaternaire 53, 79–106.

Schaefer, J.M., Denton, G.H., Barrell, D.J.A., Ivy-Ochs, S., Kubik, P.W., Andersen, B.G., Phillips, F.M., Lowell, T.V., Schlüchter, C., 2006. Near-synchronous interhemispheric termination of the last glacial maximum in mid-latitudes. Science 312, 1510–1513.

Schaefer, J.M., Denton, G.H., Kaplan, M., Putnam, A., Finkel, R.C., Barrell, D.J.A., Andersen, B.G., Schwartz, R., Mackintosh, A., Chinn, T., Schlüchter, C., 2009. High-frequency Holocene glacier fluctuations in New Zealand differ from the northern signature. Science 324, 622–625.

Shulmeister, J., Fink, D., Augustinus, P.C., 2005. A cosmogenic nuclide chronology of the last glacial transition in North-West Nelson, New Zealand – new insights in Southern Hemisphere climate forcing during the last deglaciation. Earth and Planetary Science Letters 233, 455–466.

Staiger, J., Gosse, J., Toracinta, R., Oglesby, B., Fastook, J., Johnson, J., 2007. Atmospheric scaling of cosmogenic nuclide production: climate effect. Journal of Geophysical Research 112, BO2205.

Stone, J.O., 2000. Air pressure and cosmogenic isotope production. Journal of Geophysical Research 105, 23753–23759.

Stuiver, M., Polach, H.A., 1977. Discussion of reporting ^{14}C data. Radiocarbon 19, 355–363.

Sutherland, R., Kim, K., Zondervan, A., McSaveney, M., 2007. Orbital forcing of mid-latitude Southern Hemisphere glaciation since 100 ka inferred from cosmogenic nuclide ages of moraine boulders from the Cascade Plateau, southwest New Zealand. Geological Society of America Bulletin 119, 443–451.

Telford, R.J., Heegaard, E., Birks, H.J.B., 2004. The intercept is a poor estimate of a calibrated radiocarbon age. The Holocene 14, 296–298.

Thompson, W., Fowler, B., Dorion, C., 1999. Deglaciation of the northwestern white mountains, New Hampshire. Géographie Physique et Quaternaire 53, 59–77.

Tippett, J.M., Kamp, P.J.J., 1993. Fission track analysis of the late Cenozoic vertical kinematics of continental Pacific crust, south Island, New Zealand. Journal of Geophysical Research 98, 16,119–16,148.

Vandergoes, M.J., Dieffenbacher-Krall, A.C., Newnham, R.M., Denton, G.H., Blaauw, M., 2008. Cooling and changing seasonality in the southern Alps, New Zealand during the Antarctic cold reversal. Quaternary Science Reviews 27, 589–601.

Youngson, J., Bennett, E., Jackson, J., Norris, R., Raisbeck, G., Yiou, F., 2005. "Sarsen Stones" at German Hill, Central Otago, New Zealand, and their potential for in situ cosmogenic isotope dating of landscape evolution. Journal of Geology 113, 341–354.

Please cite this article in press as: Putnam, A.E., et al., In situ cosmogenic ^{10}Be production-rate calibration from the Southern Alps, New Zealand, Quaternary Geochronology (2010), doi:10.1016/j.quageo.2009.12.001